



저작자표시-비영리-변경금지 2.0 대한민국

이용자는 아래의 조건을 따르는 경우에 한하여 자유롭게

- 이 저작물을 복제, 배포, 전송, 전시, 공연 및 방송할 수 있습니다.

다음과 같은 조건을 따라야 합니다:



저작자표시. 귀하는 원저작자를 표시하여야 합니다.



비영리. 귀하는 이 저작물을 영리 목적으로 이용할 수 없습니다.



변경금지. 귀하는 이 저작물을 개작, 변형 또는 가공할 수 없습니다.

- 귀하는, 이 저작물의 재이용이나 배포의 경우, 이 저작물에 적용된 이용허락조건을 명확하게 나타내어야 합니다.
- 저작권자로부터 별도의 허가를 받으면 이러한 조건들은 적용되지 않습니다.

저작권법에 따른 이용자의 권리는 위의 내용에 의하여 영향을 받지 않습니다.

이것은 [이용허락규약\(Legal Code\)](#)을 이해하기 쉽게 요약한 것입니다.

[Disclaimer](#)

공학박사학위논문

**A study on shear banding instability and
mass/momentum transport of particulate suspensions
under non-uniform flow field**

입자계 현탁액의 shear banding instability 및 불균일 유동장
하에서의 물질, 운동량 전달에 대한 연구

2019년 02월

서울대학교 대학원

화학생물공학부

진 호 원

Abstract

A study on shear banding instability and mass/momentum transport of particulate suspensions under non-uniform flow field

Jin, Howon

School of Chemical and Biological Engineering

The Graduate School

Seoul National University

Non-uniform flow, where the velocity gradient is spatially inhomogeneous, gives rise to many complex transport phenomena in particulate systems. Though the non-uniform flow is unavoidable in many important manufacturing processes or micro fluidic flows of particulate system, relatively few studies have been focused on dynamics of particles under such inhomogeneous flow, because of limited approaches and analysis on non-uniform fields. In this thesis, mass and momentum transport of particles under non-uniform flow field are investigated, by using both theoretical and numerical approaches.

First, mass transport due to the gradient of shear rate, which lead to

the shear banding instability, is investigated for hard sphere glasses. The origin of the mass flux is found to be shear-distorted pair correlation function during deformation, and the transport coefficients are derived in terms of pair-correlation function. The values of the correlation functions under various flow conditions are estimated by using Brownian dynamics simulation, in order to obtain explicit expression of the transport coefficients as a function of shear rate and concentration. Linear stability analysis gives stability criteria which comes from the obtained transport coefficients, and the criteria is compared to experimental results from previous researchers. Lastly, the numerical simulation of shear banding flow is performed and the unstable dynamics are analyzed.

Second, the non-local of particulate suspension is investigated, which is the momentum transport due to non-uniform flow field. As a preliminary step, the non-local stress of dilute hard sphere suspension is derived by applying spatial Taylor-expansion of stress tensor under inhomogeneous flow field. The calculation gives rise to the Einstein analogous expression of non-local stress. In order to extend the result of dilute case to more complex material, again, Brownian dynamics simulation is performed. In the Brownian dynamics simulation external extra force which is sinusoidally varying in space is applied to each particle to achieve well controlled non-uniform flow of the suspension. During the simulation, the local shear rate profiles and stress profiles are estimated, and the profiles are least-squares fitted based on the

constitutive model with the non-local stress contribution. As a results, fore-obtained Einstein analogy, the proportionality between viscosity and non-local stress coefficient is again verified.

Key words: shear banding instability, non-uniform flow field, particulate suspension, mass and momentum transport phenomena, constitutive equation, Brownian dynamics simulation, micro structure

Student Number: 2012-20980

Contents

Abstract.....	i
List of Figures.....	vi
Chapter 1 Introduction.....	1
Chapter 2 Shear rate gradient induced mass flux and flow instability of hard sphere glasses.....	6
2.1. Introduction.....	7
2.2. Modeling and numerical methods.....	11
2.2.1. The origin of the SCC instability.....	11
2.2.2. Brownian dynamics simulation.....	21
2.2.3. Equation of motion.....	25
2.2.3.1. The advection–diffusion equation.....	25
2.2.3.2. The equation of motion for suspension velocity.....	27
2.3. Results and discussion.....	32
2.3.1 Pair–correlation function from BD simulation.....	32
2.3.2. Linear stability analysis and stability diagram.....	43
2.3.3 Numerical results for concentration– and flow–profiles.....	51

Chapter 3 Non-local stresses in highly non-uniformly flowing suspensions: The shear-curvature viscosity ...	65
3.1. Introduction.....	66
3.2. Non-local stresses for dilute suspensions: the Einstein analog for the shear-curvature viscosity.....	70
3.3. An effective medium approximation for the shear-curvature viscosity.....	77
3.4 Brownian dynamics simulation.....	79
3.5. Results and discussion.....	84
 Chapter 4 Concluding remark.....	 95
 Reference.....	 99
 국문초록.....	 103
 Curriculum Vitae.....	 105

List of Figures

Figure 2.1. A comparison between the simulated contact values of the equilibrium pair-correlation function (the data points) and the Carnahan - Starling Eq. (21) (the solid line)34

Figure 2.2. The difference Δg between the angular averaged pair-correlation function and the equilibrium pair-correlation function as a function of the inter-particle separation in units of the particle radius a . The inset shows the equilibrium pair-correlation function. The volume fraction is 55%.....36

Figure 2.3. (a) The pair correlation function for a volume fraction of 45% in equilibrium, without shear flow. The color code indicates the value of the pair-correlation function (blue is a low value and red is a high value). (b) the same as in (a), but now for a shear rate corresponding to a Peclet number equal to $\tilde{\gamma} = 0.5$. The arrows indicate the compressional and extensional directions. (c) The difference between the pair correlation functions under shear in (b) and without shear in (a). The blue color code now corresponds to a negative value and the red color code corresponds to a positive value.....37

Figure 2.4. (a) The contact value g_{iso}^c of the isotropic part of the pair–correlation function as a function of the Peclet number for various volume fractions. The data points are BD–simulation results for $\phi = 0.25$ (the lower set of data points) up to $\phi = 0.55$ (the upper set of data points), increasing in steps of 0.05. (b) The difference Δg_{iso}^c between the isotropic contact values of the pair–correlation function of the sheared and unsheared equilibrium system as a function of the Peclet number for various volume fractions. The slope of the straight lines in this double–logarithmic plot is equal to the exponent m in Eq. (22). (c) The exponent m as a function of the volume fraction. The solid curve is the second order polynomial in Eq. (22). (d) The quantity $H \equiv \Delta g_{\text{iso}}^c / \tilde{\gamma}^m$ as a function of $1 - \phi / \phi_m$ on a double–logarithmic scale. The slope of the straight line is equal to the exponent $-s$ in Eq. (23). Some of the data points fall right on top of each other, so that they are not visible in this plot.....38

Figure 2.5. (a) The dimensionless quantity Γ / K^2 and (b) the dimensionless (negative) growth rate Γ as a function of the squared dimensionless wave vector $K = ka$. Here, $S = 2$ and $C = 200$ (solid curves) and $C = 400$ (dashed–dotted lines).....47

Figure 2.6. The stability diagrams in the shear-rate versus the concentration plane: (a) for $\phi < \phi_g$ and (b) for $\phi > \phi_g$. The thick line marks the transition from stable to unstable (where $S=1$). The iso- S lines are indicated by their corresponding values for S , whose curves are separated by a color code (red is a relatively high value of S and blue is a low value). The data points are experimental data for sterically stabilized PMMA particles: the white data points are for particles with a radius of 138 nm and the black data points for 150 nm, taken from [23].....49

Figure 2.7. The cylindrical Couette geometry. The radius of the inner, rotation cylinder is R_1 , the outer radius of the stationary cylinder is R_2 . The gap width is chosen to be 1000 times the radius a of the spherical colloids, and $R_1/R_2 = 0.98$54

Figure 2.8. Stationary profiles for a volume fraction of 0.60, well within the glass. (a) Velocity profiles: the dashed blue curve is for a Newtonian fluid, the blue solid line is for a stable initial state where the applied dimensionless stress is equal to 200, and the red solid curve is for an unstable initial state with an applied stress equal to $\tilde{\Sigma}(R_1) = 50$. The corresponding Peclet numbers are 1.0 and 0.0078, respectively. Velocities are normalized with respect to the

velocity of u_{wall} of the rotating inner cylinder. (b) The difference of the flow velocity of a Newtonian fluid and the local velocity. (c) The position dependent volume fraction.....58

Figure 2.9. Stationary profiles starting from a stable state, for a concentration just above the glass transition, for an overall volume fraction of $\phi = 0.582$. (a) The velocity profile and (b) the volume fraction, for applied stresses of $\tilde{\Sigma}(R_1) = 14$ (the red curves) and 20 (the blue curves). The resulting apparent Peclet numbers $\tilde{\gamma}$ are indicated in the figure. The velocities are normalized by the velocity of the rotating inner cylinder u_{wall} . The black dashed line is the profile for a Newtonian fluid.....60

Figure 2.10. Temporal evolution of (a) the concentration profile, (b) of the velocity profile, and (c) of the apparent Peclet number. The various times $\tilde{t} = tD_0 / a^2$ are indicated in (b). The overall volume fraction of 0.60, and the applied stress of $\tilde{\Sigma}(R_1) = 50$, of which the stationary profiles are given in Figure 2.8, (the red curves).....64

Figure 3.1. Insertion of a sphere into a flowing solvent (the gray sphere before insertion and the blue sphere after immersion). This sketch pictures the solvent's flow velocity in the $x -$

direction (the blue solid lines) that varies in the y – direction for (a) a solvent flow velocity with a constant shear rate and (b) for a spatially varying shear rate. The red lines schematically depict equidistant stress areas corresponding to the flow fields generated after insertion of the sphere. The corresponding expressions for the suspension stress tensor are indicated in the figures. The additional curved flow in (b) gives rise to an additional stress equal to $-2\kappa\nabla^2\mathbf{D}$ 76

Figure 3.2. The relative viscosity of a homogeneously sheared system with a volume fraction of $\tilde{\phi} = 0.3$ as a function of the Peclet number $\bar{\gamma}$. Blue data points are simulation results, and the black solid line is a fit to the empirical Carreau–Yasuda function (54). The values of the fitting parameters are $\eta_q = 5.6$, $\eta_\infty = 0$, $\lambda = 4.87$, and $m = 0.24$ 86

Figure 3.3. (a) The velocity profile obtained from a simulation with $\bar{\gamma}^* = 0.5$ and with a wave number equal to $k = 4\pi/L$. The black solid line corresponds to a linear flow with a constant shear rate $\bar{\gamma}^* = 0.5$, and the red line is a sinusoidal fit to the actual velocity profile. The inset shows the corresponding plot for $\Delta v^* = v^* - \bar{\gamma}^* y^*$, where the open data points are simulation data. (b) The shear rate profile obtained from

numerical differentiation of the data points shown in the inset in (a). The red solid line is obtained from the fitted curve in (a), which corresponds to Eq. (57).....89

Figure 3.4. (a) The local shear stress σ^* under inhomogeneous shear flow for an average shear rate $\bar{\dot{\gamma}}^* = 0.5$ and for four different wave numbers $k = 2n\pi / L$ with $n = 1, 2, 3, 4$, corresponding to the black, green, blue, and red simulation data points, respectively. The solid lines are global fits for all wave vectors simultaneously to Eq. (62). (b) The simulated stress profile as in (a) for $n = 4$, where now the solid line is the best global fit result with the neglect of non-local stress contributions. The inset shows the difference between the fitting result for the stress profile with and without contributions from the non-local stress.....92

Figure 3.5. (a) Results of the least-square fits for Λ_0 , C_1 , and C_2 (the red stars, green circles, and blue triangles, respectively) for three values of the Peclet number $\bar{\dot{\gamma}}^* = 0.2, 0.5, \text{ and } 1.0$. The horizontal red line is the weighted average of the three data points for Λ_0 . (b) The relative viscosity (in blue) as compared to the relative viscosity η_κ^*

as obtained from the numerical values for $\Lambda_0 = 3.8$ and $a/R = 2.07$ (in red) according to the effective-medium approximation in Eq. (46).....94

Chapter 1.

Introduction

Particulate soft matter systems, such as colloid, gel or glasses are widely used in a lot of industrial applications. Also, these systems are attracting scientific interests due to their complex behaviors, which are various interaction between particles, thermal motion and hydrodynamic interaction via suspending medium [1–3]. Consequently, there have been extensive studies on microstructure of suspension, rheological properties or interaction with flow field for several decades.

Many studies investigated the properties of particulate suspensions by using rheometric devices, which offer uniform and well-controlled flow field, for example, steady/ start-up / oscillatory shear flows. So far, a lot of successful analysis on the behaviors of particulate suspension has been reported, for example, phase behaviors of suspension under various flow condition, mechanism of shear thinning/thickening of suspension, yielding and structural evolution under shear flow and so on [4].

However, materials would undergo much complex flow fields in real industrial situation, which is not spatially uniform. Moreover, some complex materials are inherently unstable, which cannot form stable homogeneous flow, so that the flow would be separated into several different states [5]. The highly non-uniform flow field gives rise to additional complicated behaviors, for example, mass transport due to the gradient of deformation rate, or extra contribution to stress, which is

so-called non-local stress [6,7]. Thus, it is important to understand a behavior of particulate suspension in non-uniform or unstable flow field.

The example of non-uniform flow covered by this thesis is a shear banding instability which is shear-induced phase separation occurring in Couette flow, shear flow through the space between parallel plates [5]. The shear banding instability results in sharp interface between each 'shear bands', where the gradient of shear rate is extremely high. In this highly non-uniform region, aforementioned mass and momentum transport phenomena play an important role.

In addition to the shear banding instability, microchannel flow is another famous example of non-uniform flow, which is recently spotlighted for various applications [8,9]. In the microchannel flow, there is huge gradient of flow profile due to the small length scale and stick/slip boundary condition. Recently, it has been reported that the flow profile cannot be predicted by classical constitutive models, which do not incorporate a concept of non-local stress, due to such high inhomogeneity of the flow field [10].

Though there are numerous reports about the effect of non-uniform flow in many soft matter systems, relatively few studies have focused on the microscopic origin of such non-local phenomena, especially for particulate suspension. The reason is, supposedly, due to the difficulties in controlling the inhomogeneity of flow field and measuring the

response of the system. Only recently, some limited approaches on investigating non-local behaviors of soft matter system, by using optical visualization technique [11], however, still not clearly successful to elucidating the physical origins.

In this thesis, to avoid the difficulties of measuring and investigating local spatially varying quantities in non-uniform field, theoretical modeling and particle simulation method are used, which allow simplification of complicated flowing system by applying adequate postulates, or controlling inhomogeneity of the flow itself.

Firstly, mass transport of particle in colloidal glasses due to non-uniform flow field is investigated in chapter 2. In this work, explicit relation between the transport coefficients and microstructure of the particles is developed by modeling the force exerted on the particle under inhomogeneous flow field, in terms of shear-distorted pair-correlation function. And then, Brownian dynamics simulation is performed to calculate the pair-correlation function of hard sphere system under various shear rate and concentration. Based on both results, the stability criteria are constructed and compared with experimental result. Moreover, full equation of motions, both mass and momentum conservation equation are solved together and the results are analyzed. Here, the non-local stress, which will be discussed in chapter 3, plays important role in the initial unstable dynamics of flow and

development of the stationary states.

Secondly, to elucidate the presence of non-local stress of particulate suspension and its effect on non-uniform flow of the suspension, hydrodynamic modeling and Brownian dynamics simulation are used. In the modeling part, the non-local stress term is derived for dilute hard sphere suspension, by using the method of reflection and systematic expansion on the inhomogeneous flow field. The result is found to be analogous to Einstein viscosity of dilute hard sphere suspension. To expand the results for more complicated systems, Brownian dynamics simulation is again applied. In this simulation, small spatial perturbation is imposed on the shear flow of the suspension. And then, the response of the suspension, the local stress profiles are estimated by varying the wave-vector of the perturbation. By fitting the local stress profile based on the modeling result, which contains Einstein analogy, the non-local stress term and its coefficient are measured.

In summary, the objectives of this thesis are, understanding the mass and momentum transport phenomena of particulate suspensions under non-uniform flow field, by using modeling and simulation approaches, and quantitatively analyzing the effect of such transport phenomena on flow instability of the suspensions, so that hopefully it helps the fundamental understanding of the complex flow of suspension in many processes.

Chapter 2.

Shear rate gradient induced mass flux and
flow instability of hard sphere glasses

2.1 Introduction

As mentioned in the chapter 1, an example of shear banding instability which particulate system can undergo will be covered in this chapter. In classical point of view in the rheometry, due to the fact that the shear stress is constant everywhere in planar Couette flow, the shear rate may also be constant when materials sheared inside the Couette. However, it has been reported that some materials cannot maintain the uniform single phase and separated into multiple ‘shear bands’ [5]. The shear banding instabilities can be classified to 3 kinds, by the alignment direction of shear bands or the origin of the flow instability, which are gradient banding, vorticity banding and shear rate gradient–concentration coupling instability [12].

The most well–studied shear banding instability is the gradient banding, which shows shear bands aligned in velocity–gradient plane of Couette flow. This type of instability is observed, for example, in worm–like micellar systems, entangled polymeric systems, micellar cubic phases, transient networks, supra–molecular polymer solutions, liquid crystalline polymers, and surfactant solutions [13–15]. The gradient–banding instability is the result of a decreasing stress of the homogeneously sheared matters with the increasing shear rate. Any system that exhibits very strong shear–thinning behavior that is necessary to give rise to such a decrease of the stress will exhibit gradient banding.

A second relatively well understood instability is the so-called vorticity–banding instability, which leads to the formation of alternating bands which are stacked along the vorticity direction. It has been observed, for example, in systems of multi–lamellar vesicles, worm–like micelles, dispersions of rod–like colloids, nano–tube suspensions, and weakly aggregated colloidal suspensions [16]. There are several possible scenarios for the vorticity–banding instability, depending on the system under consideration. A possible mechanism underlying this instability is that hoop stresses are generated through the non–linear elastic deformation of the mesoscopic objects that are present in the dispersion [17], similar to the Weissenberg effect in polymeric systems. Instead of non–linear elastic deformation of polymer chains, mesoscopic objects are now elastically deformed, like worm–like micelles, aggregates, or inhomogeneities formed during the initial stages of phase separation. Elastic instabilities have been discussed at length in [18]. Other scenarios for the formation of vorticity bands is that, after the formation of interfaces due to gradient–banding, the interface between the gradient–bands is unstable, where undulation of the interface subsequently leads to band–formation along the vorticity direction [19], or where the high shear–rate branch is unstable [20].

A third instability, which is the objectives of this chapter, is shear rate gradient – concentration coupling (SCC–) instability, which has been discussed in [20, 21] within a phenomenological approach. The behavior of SCC instability is similar with the gradient banding, as SCC instability

also shows shear bands in velocity–gradient plane. However, the physical origin of the SCC instability differs from the gradient banding. In the SCC instability, an essential ingredient here is that a mass flux is induced by spatial gradients of the local shear rate. However, the previous studies postulate either a shear–rate chemical potential or osmotic pressure, and do not address the microscopic origin of the SCC–instability. The unexplained microscopic origin of the SCC–instability is probably the reason why this type of instability has hardly been pursued. But recently, there has been reported that a paper in which experiments on colloids are interpreted as being the result of the SCC–instability [23], where the driving force for the shear rate gradient induced mass flux is formulated in terms of a shear rate dependent osmotic pressure. Such a shear rate dependent osmotic pressure has indeed been observed in experiments [24–26]. Brownian dynamics simulations on hard–sphere suspensions have been performed to quantify the shear rate dependence of this generalized osmotic pressure [27].

In the present paper the microscopic origin of the shear rate gradient induced mass flux due to direct inter–colloidal interactions is discussed in section 2.2.1, which can be formulated in terms of a shear rate dependent osmotic pressure. This leads to expressions for concentration and shear rate dependent transport coefficients in terms of the shear–distorted pair correlation function. Brownian dynamics simulations for hard sphere suspensions are presented in section 2.2.2, from which

explicit expressions for these transport coefficients are obtained as functions of the concentration and shear rate. This in turn allows formulation of the advection–diffusion equation, which couples to the Navier–Stokes equation, as discussed in 2.2.3. Stability diagrams are constructed in Section 2.3.2 on the basis of these equations of motion. The coupled advection–diffusion equation and the Navier–Stokes equation are solved numerically for Couette geometry in section 2.3.3.

In addition, an essential non–local contribution to the stress that accounts for stresses resulting from large gradients in the suspension flow velocity, is adopted. This non–local contribution stabilizes the system against the unphysical arbitrary fast growth of large wave–vector Fourier components, and renders the numerical algorithms stable. The resulting kinetics and stationary states are discussed in terms of flow–velocity profiles and concentration profiles.

2.2 Modeling and numerical methods

2.2.1 The origin of the SCC instability

The self-amplifying mechanism that gives rise to the Shear rate gradient – Concentration Coupling (SCC–) instability can be understood intuitively as follows. [12, 16, 21, 23, 28] Consider a Couette cell, where the shear rate near the outer cylinder is smaller as compared to the inner cylinder. When a mass flux is induced by spatial gradients of the shear rate towards regions of smaller shear rates, mass will be transported towards the outer cylinder. The increase of concentration near the outer cylinder leads to an increase of the local stress. The response of the system is to decrease the stress by lowering the local shear rate. This amplifies the spatial gradients of the shear rate, and leads to an enhanced mass flux towards the outer cylinder. The enhanced mass flux in turn gives rise to an even larger concentration, resulting in an even lower local shear rate. This is the self-amplifying mechanism that underlies the SCC–instability. A stationary state is reached once the diffusive mass flux due to existing concentration gradients cancels the shear–gradient induced mass flux.

The SCC–instability has not been further analyzed after the original publications, [21] and [29], which are probably due to the ad hoc introduction of a lift force and a shear–rate dependent chemical potential, respectively, of which the origin is uncertain. The aim of this section is to elucidate the origin of the shear–rate dependence of the relevant

transport coefficients. A microscopic derivation of the mass flux from first principles will be discussed, and the origin of the shear–gradient contribution to the mass flux will be unambiguously identified. As expected, mass fluxes must be formulated in terms of a generalized osmotic pressure, as has been assumed in the analysis in [23]. This allows for the microscopic modeling of the advection–diffusion equation, including the mass flux induced by spatial gradients of the shear rate.

The driving force for mass transport induced by shear rate gradients considered here is not to be confused with the phenomenon described in [30, 31], where the mass flux is entirely described in terms of the shear–rate dependence of the Fick’s diffusion coefficient. Here, no explicit shear rate gradient contribution appears in the diffusion equation which is necessary for the SCC–instability. Mass transport for such “shear–induced diffusion processes” is only significant for large particles, and does not play a role in the SCC–instability as found in [23].

The general form of the diffusion–advection equation for the number density ρ of colloids, which undergoes a flow \mathbf{u} , reads (with the neglect of hydrodynamic interactions between the colloidal particles),

$$\frac{\partial \rho}{\partial t} + \nabla \cdot (\rho \mathbf{u}) = D_0 \nabla^2 \rho - \beta D_0 \nabla \cdot \mathbf{B} \quad (1)$$

where $D_0 = k_B T / \xi_0$ is the free single–particle diffusion coefficient and ξ_0 is the friction coefficient, while interactions between colloidal

particles are accounted for by the body force \mathbf{B} . The diffusion Eq. (1) complies with a continuity equation with a mass flux $\mathbf{j} = \rho \mathbf{v}$, where the thermally averaged velocity \mathbf{v} of a colloidal particle is equal to,

$$\mathbf{v} = \mathbf{u} + \frac{1}{\xi_0} \left(-k_B T \nabla \ln \rho + \frac{\mathbf{B}}{\rho} \right) \quad (2)$$

This expresses force balance on the diffusive time scale, where the friction force $\xi_0 \mathbf{v}$ balances with the Brownian force (the first term between the square brackets) and the body force \mathbf{B} which is due to colloid–colloid interactions. The body force that is due to direct inter–colloidal interactions is equal to,

$$\mathbf{B}(\mathbf{r}, t) = - \left\langle \sum_{i=1}^N [\nabla_i \Phi] \delta(\mathbf{r} - \mathbf{r}_i) \right\rangle, \quad (3)$$

where Φ is the potential energy of an assembly of N colloidal particles and δ is the delta–distribution, with \mathbf{r}_i being the position coordinate of colloid i .

The above general form of the diffusion equation is also given in [32], where the body force is referred to as “the particle contribution to the stress”. The body force that includes forces on the colloidal particles and the solvent molecules is the body force that appears in the Navier–Stokes equation, and thus relates to the total stress.

Now it will be shown how the expression (3) for the body force gives rise to a contribution in the mass flux that is proportional to $\nabla \dot{\gamma}$ where $\dot{\gamma}$ is the local shear rate. First of all, the ensemble average in Eq. (3) is

written in terms of an integral with respect to the probability density function P_N of the position coordinates of N spherical colloids,

$$\mathbf{B}(\mathbf{r}, t) = -N \int d\mathbf{r}_1 \dots \int d\mathbf{r}_N P_N \nabla_1 \Phi \delta(\mathbf{r} - \mathbf{r}_1).$$

For a potential Φ that is a pair-wise additive sum of pair-interaction potentials V , it is readily found that,

$$\mathbf{B}(\mathbf{r}, t) = -N(N-1) \int d\mathbf{r}_2 P_2(\mathbf{r}, \mathbf{r}_2, t) \nabla V(|\mathbf{r} - \mathbf{r}_2|),$$

where,

$$P_2(\mathbf{r}, \mathbf{r}_2, t) = \int d\mathbf{r}_3 \dots \int d\mathbf{r}_N P_N(\mathbf{r}_1, \mathbf{r}_2, \dots, \mathbf{r}_N, t).$$

Introducing the pair-correlation function g ,

$$P_2(\mathbf{r}, \mathbf{r}_2, t) = \frac{1}{N(N-1)} \rho(\mathbf{r}, t) \rho(\mathbf{r}_2, t) g(\mathbf{r}, \mathbf{r}_2, t, [\rho, \dot{\gamma}]),$$

where the notation $[\rho, \dot{\gamma}]$ is used to indicate functional dependence of the pair-correlation function on the density and shear rate (for the inhomogeneous systems under consideration), the body force on the colloidal particles can be written as,

$$\mathbf{B}(\mathbf{r}, t) = -\rho(\mathbf{r}, t) \int d\mathbf{r}_2 \rho(\mathbf{r}_2, t) g(\mathbf{r}, \mathbf{r}_2, t, [\rho, \dot{\gamma}]) \nabla V(|\mathbf{r} - \mathbf{r}_2|).$$

Since the potential restricts the integration range to distances $|\mathbf{r} - \mathbf{r}_2|$ less than the range R_v of the pair-interaction potential, only the short-ranged shear-induced distortion of the pair-correlation needs be considered. For these small distances the shear-flow distortion of the pair-correlation function is to a good approximation affine, so that,

$$\begin{aligned}
g(\mathbf{r}, \mathbf{r}_2, t, [\rho, \dot{\gamma}]) &= g^{\text{eq}}(\mathbf{r}, \mathbf{r}_2, [\rho, \dot{\gamma}]) + g_0(\mathbf{r}, \mathbf{r}_2, [\rho, \dot{\gamma}]) \\
&\quad + \frac{\mathbf{r} - \mathbf{r}_2}{|\mathbf{r} - \mathbf{r}_2|} \cdot \hat{\mathbf{E}} \cdot \frac{\mathbf{r} - \mathbf{r}_2}{|\mathbf{r} - \mathbf{r}_2|} g_1(\mathbf{r}, \mathbf{r}_2, [\rho, \dot{\gamma}]),
\end{aligned} \tag{5}$$

where g^{eq} is the equilibrium pair-correlation function in the absence of shear flow, g_0 is the isotropic shear-induced distortion, and g_1 characterizes the anisotropic affine distortion of the pair-correlation function. Furthermore, $\hat{\mathbf{E}}$ is the symmetric part of the velocity-gradient tensor divided by the local shear rate. As expression (5) for the pair-correlation function assumes an affine distortion, this expression is accurate only when the Peclet number corresponding to the radius of the colloidal spheres is not larger than order unity. For a simple shear flow in the x-direction and with y the gradient direction, this tensor is equal to,

$$\hat{\mathbf{E}} = \frac{1}{2} \begin{pmatrix} 0 & 1 & 0 \\ 1 & 0 & 0 \\ 0 & 0 & 0 \end{pmatrix}.$$

The shear rate and colloid density vary only a little over distances less than R_V , so that the density appearing in the integral (4) for the body force, $\rho(\mathbf{r}_2, t)$ can be Taylor expanded around \mathbf{r} to a leading order in gradients,

$$\rho(\mathbf{r}_2, t) = \rho(\mathbf{r}, t) + (\mathbf{r}_2 - \mathbf{r}) \cdot \nabla \rho(\mathbf{r}, t). \tag{6}$$

For the same reason, the various contributions to the pair-correlation function in Eq. (5) are approximately equal to those in a homogeneous

system, with the density and shear rate taken in between the positions \mathbf{r} and \mathbf{r}_2 . For example,

$$g_0(\mathbf{r}, \mathbf{r}_2, [\rho, \dot{\gamma}]) = \bar{g}_0(|\mathbf{r} - \mathbf{r}_2|, \bar{\rho}, \bar{\dot{\gamma}}), \text{ with } \bar{\rho} = \rho\left(\frac{1}{2}(\mathbf{r} + \mathbf{r}_2), t\right),$$

$$\text{and } \bar{\dot{\gamma}} = \dot{\gamma}\left(\frac{1}{2}(\mathbf{r} + \mathbf{r}_2), t\right),$$

and similar to g^{eq} and g_1 . Here, the overbar on \bar{g}_0 is used to indicate that this is the correlation function of a homogeneous system with density $\bar{\rho}$ and shear rate $\bar{\dot{\gamma}}$. Since the temporal evolution of the long wave length density and shear rate variations are much slower than the relaxation time of the pair-correlation function for distances less than R_v , the pair-correlation function adjusts itself instantaneously to its local stationary form. The time dependence of the pair-correlation function is therefore entirely due to the time dependence of the local density and shear rate. Within a leading order gradient expansion, following is obtained ($\mathbf{R} = \mathbf{r}_2 - \mathbf{r}$),

$$g_0(\mathbf{r}, \mathbf{r}_2, [\rho, \dot{\gamma}]) = \bar{g}_0(R|\rho, \dot{\gamma}) + \frac{1}{2} \frac{\partial \bar{g}_0(R|\rho, \dot{\gamma})}{\partial \rho} \mathbf{R} \cdot \nabla \rho + \frac{1}{2} \frac{\partial \bar{g}_0(R|\rho, \dot{\gamma})}{\partial \dot{\gamma}} \mathbf{R} \cdot \nabla \dot{\gamma}, \quad (7)$$

and similar to g^{eq} (for which the shear rate dependence is of course absent) and g_1 . Here, ρ and $\dot{\gamma}$ are now understood to denote the local density and shear rate (omitting the now overbar notation). Substitution of Eq. (6) and (7) into Eq. (4) for \mathbf{B} , and performing the angular integrations gives,

$$\mathbf{B}(\mathbf{r}, t) = - \left[\frac{\partial P_0(\rho, \dot{\gamma})}{\partial \rho} - k_B T \right] \nabla \rho - \frac{\partial P_0(\rho, \dot{\gamma})}{\partial \dot{\gamma}} \nabla \dot{\gamma} - \frac{\partial P_1(\rho, \dot{\gamma})}{\partial \rho} \hat{\mathbf{E}} \cdot \nabla \rho - \frac{\partial P_1(\rho, \dot{\gamma})}{\partial \dot{\gamma}} \hat{\mathbf{E}} \cdot \nabla \dot{\gamma}, \quad (8)$$

up to the leading order in spatial gradients, where,

$$P_0(\rho, \dot{\gamma}) = \rho k_B T - \frac{2\pi}{3} \rho^2 \int_0^\infty dR R^3 \frac{dV(R)}{dR} [g^{\text{eq}}(R | \rho) + \bar{g}_0(R | \rho, \dot{\gamma})], \quad (9)$$

Eq. (8) can also be written as,

$$\mathbf{B}(\mathbf{r}, t) = -\nabla[P_0(\rho, \dot{\gamma}) - \rho k_B T] - \hat{\mathbf{E}} \cdot \nabla P_1(\rho, \dot{\gamma}) \quad (10)$$

where the gradient operators act on the spatial dependence of the colloid density and shear rate. The only component of the body force of interest here is the component acting along the gradient direction, which is the contribution $-\nabla[P_0 - \rho k_B T]$, because the last term $-\hat{\mathbf{E}} \cdot \nabla P_1(\rho, \dot{\gamma})$ is acting along the flow direction, which results in more drag of particle against the flow velocity.

According to Eq. (2) and (8), the mass flux in the gradient direction is thus equal to,

$$\mathbf{j} = \rho \mathbf{u} - \beta D_0 \nabla P_0(\rho, \dot{\gamma}) = \rho \mathbf{u} - \beta D_0 \nabla \left[\frac{\partial P_0(\rho, \dot{\gamma})}{\partial \rho} \nabla \rho + \frac{\partial P_0(\rho, \dot{\gamma})}{\partial \dot{\gamma}} \nabla \dot{\gamma} \right], \quad (11)$$

where $\beta = 1/k_B T$.

The interpretation of the above result for the mass flux is as follows. From equilibrium statistical mechanics, a well-known expression for the equilibrium pressure in terms of the pair-correlation function g^{eq} reads, [33]

$$P^{\text{eq}}(\rho, \dot{\gamma}) = \rho k_B T - \frac{2\pi}{3} \rho^2 \int_0^\infty dR R^3 \frac{dV(R)}{dR} g^{\text{eq}}(R | \rho).$$

Since the correlation function relates to inter-colloidal interactions, this pressure is in fact the osmotic pressure [1]. This expression for the osmotic pressure is precisely the expression for P_0 in Eq. (9), except that the equilibrium pair-correlation function is now the shear-distorted pair-correlation function. This is why P_0 shall be referred to as a “generalized osmotic pressure”. In this sense, just like for inhomogeneous unsheared systems, the mass flux is proportional to the spatial gradient of the osmotic pressure. The shear rate dependence of this generalized osmotic pressure gives rise to the shear rate gradient contribution to the mass flux. It should be noted that this generalized osmotic pressure is different from the pressure that appears in the Navier–Stokes equation. The pressure in the Navier–Stokes equation relates to the body force that includes forces on both the colloids and the solvent molecules. The body force that appears in the advection–diffusion equation is the force that results from forces on the colloids only.

In the following, it is considered that the suspensions of hard spheres, for which the pair–interaction potential is either zero, when the cores do not overlap, or is infinite, when the cores overlap. For such hard–core interactions the integral in Eq. (9) for the generalized osmotic pressure can be evaluated in terms of the contact value of the pair–correlation function, that is, the value where the distance between two colloids is

equal to $2a$, with a being the radius of the cores. To this end the so-called cavity function $y = g \exp(\beta V)$ is introduced. This function is continuous at contact, and has the same contact value as the pair-correlation function [33]. Since $\exp(-\beta V) dV / dR = -k_B T d(\exp(-\beta V)) / dR = -k_B T \delta(R - 2a)$, with δ being the delta distribution, it follows from Eq. (9) that,

$$P_0(\rho, \dot{\gamma}) = \rho k_B T + \frac{2\pi}{3} (2a)^3 \rho^2 k_B T g_{iso}^c(\rho, \dot{\gamma}), \quad (12)$$

where $g_{iso}^c(\rho, \dot{\gamma})$ is abbreviated as (the superscript “ c ” stands for the “contact value”),

$$g_{iso}^c(\rho, \dot{\gamma}) = g^{eq}(R = 2a | \rho) + \bar{g}_0(R = 2a | \rho, \dot{\gamma}).$$

The body force along the gradient direction is, according to Eq. (10) and (12), therefore equal to,

$$\mathbf{B}(\mathbf{r}, t) = \frac{2\pi}{3} (2a)^3 k_B T \frac{\partial(\rho^2 g_{iso}^c(\rho, \dot{\gamma}))}{\partial \rho} \nabla \rho + \frac{2\pi}{3} (2a)^3 k_B T \rho^2 \frac{\partial(g_{iso}^c(\rho, \dot{\gamma}))}{\partial \dot{\gamma}} \nabla \dot{\gamma}.$$

The mass flux in Eq. (11) can now be most conveniently written as,

$$\mathbf{j} = \rho \mathbf{u} - D_{eff} \nabla \rho - \xi \nabla \dot{\gamma}, \quad (13)$$

where the effective diffusion coefficient D_{eff} is equal to,

$$D_{eff}(\rho, \dot{\gamma}) = D_0 \left(1 + \frac{2\pi}{3} (2a)^3 \frac{\partial(\rho^2 g_{iso}^c(\rho, \dot{\gamma}))}{\partial \rho} \right), \quad (14)$$

and the shear-gradient coefficient is equal to,

$$\xi(\rho, \dot{\gamma}) = D_0 \frac{2\pi}{3} (2a)^3 \rho^2 \frac{\partial g_{\text{iso}}^c(\rho, \dot{\gamma})}{\partial \rho}. \quad (15)$$

The explicit density and shear-rate dependence of these transport coefficients will be obtained by means of Brownian dynamics simulations, from which the contact values of the pair-correlation function are obtained, which then allows to analyze the transient kinetics and stationary states resulting from the SCC-instability

2.2.2 Brownian dynamics simulation

In this section, Brownian dynamics (BD) simulations are presented, in order to determine the concentration and shear-rate dependence of the contact value of the pair-correlation function under shear flow conditions. The simulation results will be used to establish the explicit concentration and shear rate dependence of the effective diffusion coefficient in Eq. (14) and the shear rate gradient coefficient (15). The governing equation for BD-simulations is the overdamped Langevin equation,

$$\mathbf{0} = \mathbf{F}_i^H + \mathbf{F}_i^P + \mathbf{F}_i^B,$$

where \mathbf{F}_i^H , \mathbf{F}_i^P and \mathbf{F}_i^B are the hydrodynamic force, the inter-particle force, and the Brownian force exerted on the i th particle, respectively. On the diffusive time scale under consideration, inertial forces can be ignored. With the neglect of hydrodynamic interactions between the colloids, the hydrodynamic force is equal to,

$$\mathbf{F}_i^H = \zeta_0(\mathbf{v}_i - \mathbf{u}(\mathbf{r}_i)),$$

where $\zeta_0 = 6\pi\eta_0 a$ is the single-particle friction coefficient (with η_0 being the shear viscosity of the solvent and a the radius of the spheres), \mathbf{v}_i is the velocity of the sphere, and $\mathbf{u}(\mathbf{r}_i)$ is the externally imposed solvent velocity at the center coordinate of the i th sphere, \mathbf{r}_i . For the inter-particle force \mathbf{F}_i^P , the overlap-preventing potential free method is

employed [27]. Here, after a move of the particles leading to core-overlap, they are forced to move back to a position where there is contact between the surfaces. The corresponding displacement is equal to (with the \mathbf{r}_{ij} vector connecting the two centers of the overlapping spheres),

$$\Delta \mathbf{r}_{ij}^{\text{overlap}} = \frac{1}{2} \frac{\mathbf{r}_{ij}}{r_{ij}} (r_{ij} = 2a), \quad r_{ij} < 2a.$$

The Brownian force \mathbf{F}_i^B is generated as a random number, with zero average and variance complying with the equipartition of kinetic energy,

$$\langle \mathbf{F}_i^B \rangle = \mathbf{0},$$

$$\langle \mathbf{F}_i^B(t) \mathbf{F}_i^B(t') \rangle = 2\zeta_0 k_B T \hat{\mathbf{I}} \delta(t-t'),$$

where $\hat{\mathbf{I}}$ is the identity tensor.

Introducing dimensionless variables by rescaling the length with the radius a , energy with $k_B T$, and time with a^2 / D_0 (the time required for a particle to diffuse over a distance equal to its own radius), the dimensionless displacement of the position of particle i is (the over-tilde symbols are used to indicate dimensionless variables),

$$d\tilde{\mathbf{r}}_i = [\tilde{\mathbf{v}}_i^\infty + \tilde{\mathbf{F}}_i^p] d\tilde{t} + \sqrt{2} \tilde{\mathbf{W}}_i, \quad (16)$$

where,

$$\tilde{\mathbf{F}}_i^p = \sum_j \Delta \mathbf{r}_{ij}^{\text{overlap}},$$

and where $\tilde{\mathbf{W}}_i$ is the random dimensionless displacement due to the Brownian force, such that,

$$\langle \tilde{\mathbf{W}}_i \rangle = 0,$$

$$\langle \tilde{\mathbf{W}}_i(t) \tilde{\mathbf{W}}_i(t') \rangle = \hat{\mathbf{I}} \delta(t - t') dt$$

Furthermore, the dimensionless imposed solvent velocity $\tilde{\mathbf{v}}_i^\infty = \tilde{\mathbf{\Gamma}} \cdot \tilde{\mathbf{r}}_i$, where the dimensionless velocity gradient tensor $\tilde{\mathbf{\Gamma}}$ has only one non-zero component, the xy -element, which is equal to the Peclet number,

$$\text{Pe} = \tilde{\gamma} = \frac{a^2}{D_0} \dot{\gamma}$$

Time integration of Eq. (16) extends over the interval $\tilde{t} = 0 - 100$ with time-steps of $d\tilde{t} = 10^{-4}$, for shear rates in the range $\tilde{\gamma} = 0.01 - 10$ and for volume fractions ranging from 0.25 to 0.55. In this concentration and shear-rate range there is no SCC instability because uniform shear flow is forced throughout the simulation domain, and crystallization is not observed (probably because nucleation requires larger systems and/or it is too slow on the time scale during which the simulations are performed). In the simulation box, $N = 3375$ particles were used under periodic boundary conditions. The number of particle, $N = 3375$ is sufficiently large, by repeating simulations with 1000 particles, leading to results that are the same to within 2%.

After the steady state is reached, the pair-correlation function $g(\mathbf{r})$

is calculated from,

$$g(\mathbf{r}) = \frac{1}{\bar{\rho}^2} \left\langle \sum_{i=1}^N \sum_{\substack{j=1 \\ j \neq i}}^N \delta(\mathbf{r} - \mathbf{r}_{ij}) \right\rangle,$$

where $\bar{\rho}$ is the average number density of particles, and the brackets denote time-averaging.

2.2.3 Equation of motion

Brownian dynamics simulations cannot be used to analyze the SCC–instability, since unrealistically large systems must be simulated to achieve this, and Navier–stokes equation for background fluid motion cannot be coupled with the forces exerted on the particles. Instead, equations of motion must be formulated which are then solved numerically. In this section the two necessary equations of motion will be formulated. In subsection 2.2.3.1, the advection–diffusion equation is stated, as obtained from the considerations in the previous sections, and in subsection 2.2.3.2, the equation of motion for the flow velocity is discussed.

2.2.3.1 The advection–diffusion equation

The advection–diffusion equation as derived in section 2.2.1 does not assume equilibrium, and is therefore also applicable within the glass state. In addition, since microstructural order in the glass is very similar to that in the fluid, the contact value for the pair–correlation function is expected to be reasonable also within the glass. The advection–diffusion equation, applicable to fluids and glasses, thus follows immediately from Eq. (13)–(15).

$$\frac{\partial \rho}{\partial t} + \nabla \cdot [\rho \mathbf{u}] = \nabla \cdot [D_{\text{eff}} \nabla \rho] + \nabla \cdot [\xi \nabla \dot{\gamma}], \quad (17)$$

where \mathbf{u} is the suspension flow velocity; the effective diffusion

coefficient in terms of dimensionless variables is equal to,

$$D_{\text{eff}}(\phi, \tilde{\gamma}) = D_0 \left[1 + 4 \frac{\partial}{\partial \phi} \left(\phi^2 g_{\text{iso}}^c(\phi, \tilde{\gamma}) \right) \right],$$

where ϕ is local volume fraction of particle, which is given as $\phi = 4\pi a^3 \rho / 3$. And the shear–gradient coefficient is equal to,

$$\xi(\phi, \tilde{\gamma}) = 18\eta_0 \frac{D_0}{k_B T} \phi^2 \frac{\partial g_{\text{iso}}^c(\phi, \tilde{\gamma})}{\partial \tilde{\gamma}}.$$

The concentration and shear–rate dependence of the contact value g_{iso}^c of the isotropic part of the pair–correlation function is specified from the result of BD–simulations.

As mentioned before, the shear–rate induced mass flux as described in [30] is entirely assumed to be due to the shear rate dependence of D_{eff} in Eq. (17) [31]. This so–called shear induced diffusion leads to significant mass transport only for very large particles, larger than several tens of microns. There is no SCC–instability without the explicit contribution from shear rate gradient induced mass transport. The equation of motion (17) is coupled to the equation of motion for the suspension flow velocity \mathbf{u} , which is discussed in the next subsection.

2.2.3.2 The equation of motion for the suspension flow velocity

Although the rheological properties of concentrated hard sphere suspensions could in principle be obtained from similar Brownian Dynamics simulations as discussed in section 2.2.2, there is an abundance of literature on simulations and rheological experiments of hard-sphere systems available to be able to construct a reliable Navier-Stokes equation. In this work, it is chosen that using this existing information to construct the Navier-Stokes equation, rather than to perform a separate Brownian Dynamics study, which would merely reproduce existing knowledge.

The inertial contribution to the Navier-Stokes equations can be neglected for the low Reynolds numbers typical for colloidal systems. Furthermore, the relaxation of the fluid velocity is very fast in comparison to the temporal evolution of the colloid concentration, which can be seen as follows. The time τ_{sw} that a shear wave needs to traverse a distance l is equal to $\rho l^2 / \eta$ (where ρ_m is the specific mass density of the suspension). A lower bound for the time needed for the colloid concentration to change over a length scale l is the time $\tau_{\text{diff}} = l^2 / D_{\text{eff}}$ needed for a colloidal sphere to diffuse over that distance. When the ratio $\tau_{\text{diff}} / \tau_{\text{sw}} = \eta / (\rho_m D_{\text{eff}})$ is large, the flow velocity is enslaved by the colloid concentration. Substitution of typical numbers (shear viscosity

10^{-2}Pas , mass density 10^3kg m^{-3} , and diffusion coefficient $10^{-11}\text{m}^2\text{s}^{-1}$) shows that this ratio is of the order 10^6 . This validates the assumption that flow is enslaved by concentration, so that the explicit time derivative in the Navier–Stokes equation can be neglected. The Navier–Stokes equation therefore reduces to,

$$\mathbf{0} = \nabla \cdot \boldsymbol{\Sigma}, \quad (18)$$

where $\boldsymbol{\Sigma}$ is the stress tensor. The standard expression for the stress tensor is $\boldsymbol{\Sigma} = \boldsymbol{\Sigma}_{\text{yield}} + \eta[\nabla\mathbf{u} + (\nabla\mathbf{u})^T]$ (“T” stands for “transposition”), where $\boldsymbol{\Sigma}_{\text{yield}}$ is the yield–stress tensor, which is zero below the glass–transition volume fraction $\phi_g = 0.58$, and where η is the shear–viscosity. Spatial variations in the pressure are absent for the flow profiles under consideration here, which are therefore omitted. This expression for the stress tensor is the result of a leading order expansion with respect to gradients in the flow velocity \mathbf{u} . In banded profiles, however, gradients may be large, so that the next higher order term in such a gradient expansion must be included. This non–local contribution to the stress turns out to be essential to be able to describe the formation of banded flow profiles, as it stabilizes the system against the arbitrary fast growth of large gradients in the flow velocity (this is shown in the linear stability analysis in section 2.3.2). This holds for gradient–banding as well as for the SCC–instability. The total stress

tensor is therefore equal to [6],

$$\boldsymbol{\Sigma} = \boldsymbol{\Sigma}_{\text{yield}} + (\eta - \kappa \nabla^2) [\nabla \mathbf{u} + (\nabla \mathbf{u})^T], \quad (19)$$

where $\kappa > 0$ is referred to as the shear–curvature viscosity. Both η and κ are functions of the concentration and shear rate, which is essentially different below and above the glass concentration. The non–local stress will be further discussed in the next chapter.

What has been neglected in the constitutive relationship in Eq. (19) are normal stresses. As the system is restricted to laminar flow within symmetric geometries like a Couette cell or parallel plates, and spatial gradients of the shear rate are essential for the SCC instability, these normal stresses are neglected. For flows in more complex geometries, where normal stresses affect the direction of flow velocities, and thereby spatial gradients in the shear rate, a more realistic constitutive relationship should be employed that includes normal stresses.

For volume fractions $\phi < \phi_g$ there is a Newtonian plateau up to Peclet numbers of approximately 0.1 to 1 up to volume fraction close to ϕ_g [27, 34–36], in agreement with the simulation data in Figure 4a. For values of Peclet numbers smaller than unity that are of interest here, within the Newtonian plateau, the viscosity in Eq. (22) is thus approximated by the zero–shear viscosity. There are several propositions that describe the concentration dependence for the viscosity of hard–sphere suspensions quite accurately, like an exponential dependence on the concentration

[37] and through generalized (Stokes–Einstein relationship [38]). Here the well-known Krieger–Dougherty relationship is used [39],

$$\eta(\phi, \tilde{\gamma}) = \eta_0 (1 - \Phi)^{-q}, \quad \phi < \phi_g,$$

for the concentration dependence of the zero–shear viscosity, where η_0 is the solvent viscosity, and where the notation,

$$\Phi = \phi / \phi_m$$

is adopted from [23] as a dimensionless concentration. The experimental values of q that are reported vary from $2.5 \times \phi_m = 1.6$ [35] to 2 [40], up to concentrations of about 0.59. A theory for barrier formation and particle hopping predicts an exponent of 9.1 in the concentration range of 0.505–0.605 [41]. Here the value $q=2$ is adopted, which describes experimental data on hard–sphere silica dispersions quite accurately. The shear–curvature viscosity diverges similarly as the viscosity at the volume fraction ϕ_m , while the range of shear rates where shear thinning occurs is similar for both [6]. Therefore, it is assumed that the same concentration dependence for the shear–curvature viscosity as for the shear viscosity,

$$\kappa(\phi, \tilde{\gamma}) = \kappa_0 (1 - \Phi)^{-q}, \quad \phi < \phi_g,$$

where κ_0 is a constant.

Contrary to fluid suspensions, there is no Newtonian plateau in hard–sphere glasses. Shear thinning immediately sets in when flow is induced

by applying a stress just above the yield stress, which is reasonably well described by a Herschel–Bulkley form of the stress, which predicts that the viscosity in Eq. (19) varies like $\sim \tilde{\gamma}^{-1/2}$ [23, 42, 43]. Therefore, the same Herschel–Bulkley form is adopted as used in [23],

$$\eta(\phi, \tilde{\gamma}) = 15 \frac{a^2}{D_0} \Sigma_{\text{yield}}(\Phi)(1-\Phi)^{1/2} \tilde{\gamma}^{-1/2}, \quad \phi > \phi_g.$$

The concentration dependence of the yield stress of hard sphere glasses is $\sim (1-\Phi)^{-p}$, where p is reported to vary between 1 and 3, while the pre-factor is equal to $k_B T / (100a^3)$ [23]. The same expression for the yield stress as in [23] will be used,

$$\Sigma_{\text{yield}} = \frac{k_B T}{100a^3} (1-\Phi)^{-p}, \quad (20)$$

which is understood to act along the flow direction. The exponent is equal to, $p=3$. The shear–curvature viscosity has again a similar shear–rate and concentration dependence as the shear viscosity,

$$\kappa(\phi, \tilde{\gamma}) = 15 \frac{a^2}{D_0} \frac{\kappa_0}{\eta_0} \Sigma_{\text{yield}}(\Phi)(1-\Phi)^{1/2} \tilde{\gamma}^{-1/2}, \quad \phi > \phi_g.$$

2.3 Results and discussion

2.3.1 Pair–correlation function from BD simulation

In this section, the concentration and shear rate dependence of the contact value of the pair–correlation function under shear flow conditions is calculated. The contact value will be used to establish the explicit expressions of the effective diffusion coefficient in Eq. (14) and the shear rate gradient coefficient (15).

Firstly, to validate the results, equilibrium simulation without flow case is compared to well–known hard sphere model. An accurate description of the contact value of the pair–correlation function for hard spheres without shear flow up to concentrations of about 45% is given by the so–called Carnahan–Starling equation [44],

$$g^{\text{eq},c}(\phi) = \frac{2-\phi}{2(1-\phi)^3}. \quad (21)$$

A comparison of the BD–equilibrium simulation results with the Carnahan–Starling equation is shown in Figure 2.1. There is a reasonable agreement, with small deviations at very high volume fractions above 45%, similar to what is found in [27]. This slight overestimation is attributed in [27] to the effective softness that is introduced in the simulations through unresolved particle overlaps.

Of interest for the calculation of the transport coefficients in Eq. (14) and (15) is the contact value of the isotropic part of the pair–correlation

function, which according to Eq. (5), is equal to the angular-averaged pair-correlation function at the core surface,

$$g_{\text{iso}}(R) = g^{\text{eq}}(R | \rho) + \bar{g}_0(R | \rho, \dot{\gamma}) = \frac{1}{4\pi} \oint d\hat{\mathbf{r}} g(\mathbf{r}),$$

where the integral ranges over the directions of \mathbf{r} .

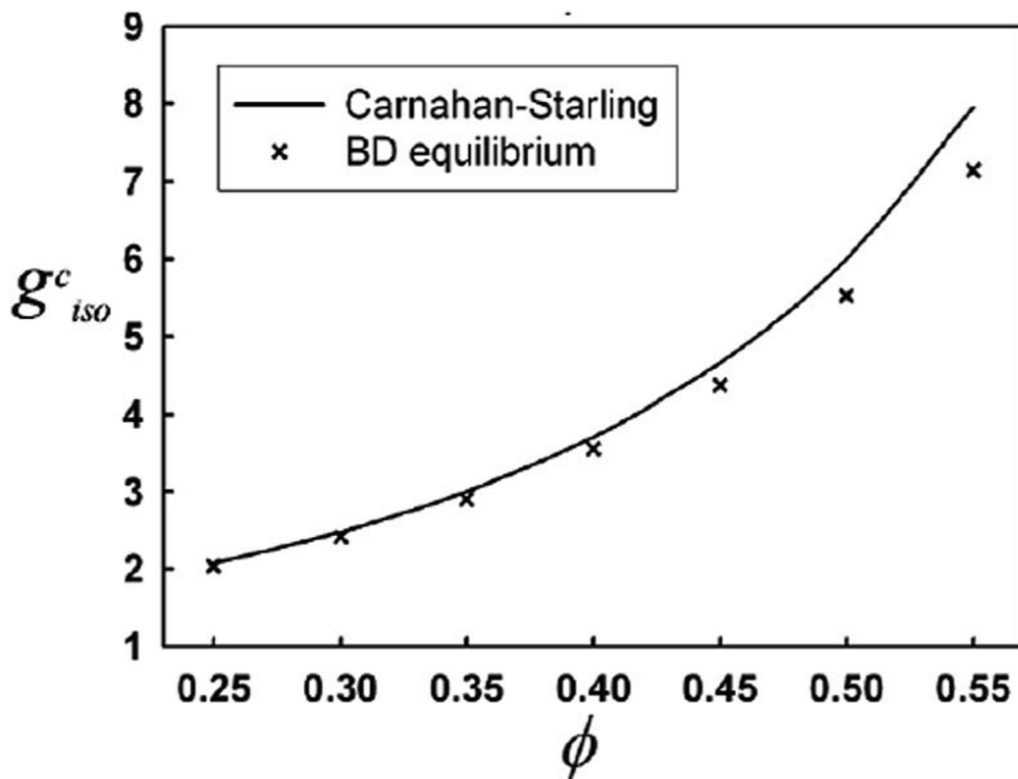


Figure 2.1 A comparison between the simulated contact values of the equilibrium pair-correlation function (the data points) and the Carnahan-Starling Eq. (21) (the solid line).

Examples of the isotropic part of the shear-distorted pair-correlation function are plotted as a function of the inter-particle separation for two shear rates in Figure 2.2. An example of the effect of shear flow on the pair-correlation function is shown in Figure 2.3, for a volume fraction of 45%. In Figure 2.3a the pair-correlation function without shear flow is shown, where the color code measures the value of the correlation function (blue is a low value and red is a high value). The dotted circle indicates the location of the core-surface. In Figure 2.3b the pair-correlation in shear flow is plotted, and in Figure 2.3c the difference between the pair-correlation function under flow and its equilibrium value is shown. There is a pronounced increase of the pair-correlation function along the compressional direction, and a clear decrease along the extensional axis, as expected. Here, note that the shear-induced stripes and peaks exhibited by the pair-correlation function as found in [27] only occur at Peclet numbers larger than about 10. Here, the analysis is restricted to Peclet numbers less than 1, for which the same oval structure for the pair-correlation function as seen in Figure 2.3 is also found in [27]. The difference Δg_{iso} between the angular averaged pair-correlation function and the equilibrium pair-correlation function is given in Figure 2.2 as a function of the inter-particle separation, for two Peclet numbers. As can be seen, the contact value is a strong function of the shear rate.

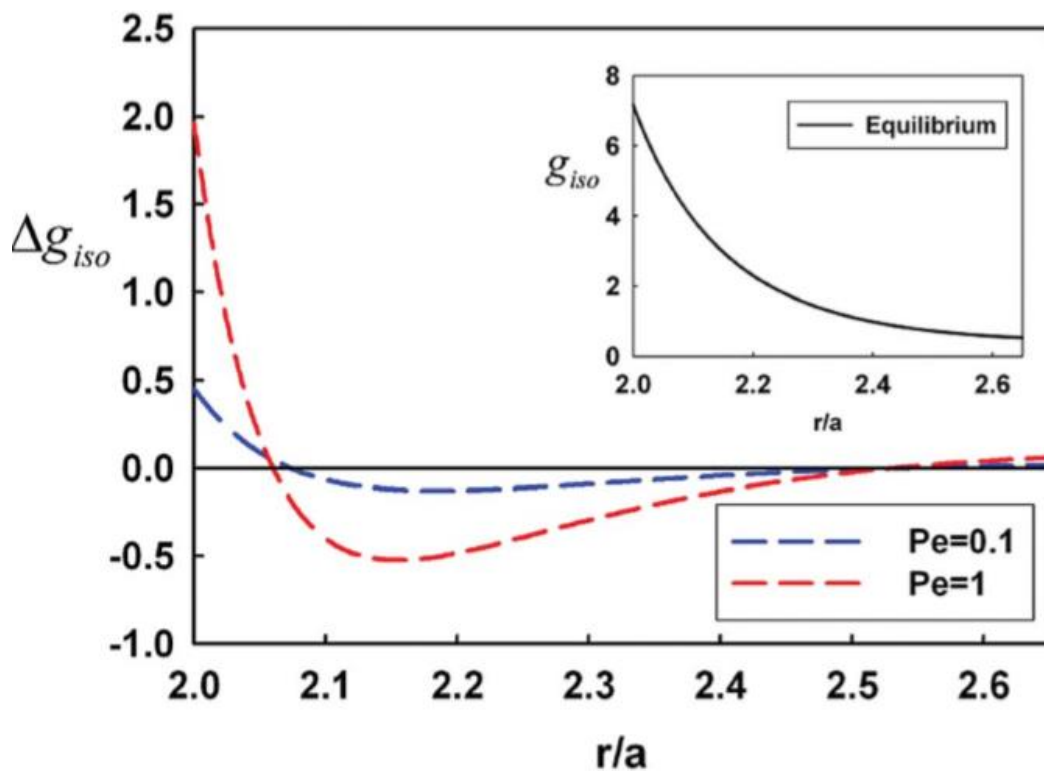


Figure 2.2 The difference Δg between the angular averaged pair-correlation function and the equilibrium pair-correlation function as a function of the inter-particle separation in units of the particle radius a . The inset shows the equilibrium pair-correlation function. The volume fraction is 55%

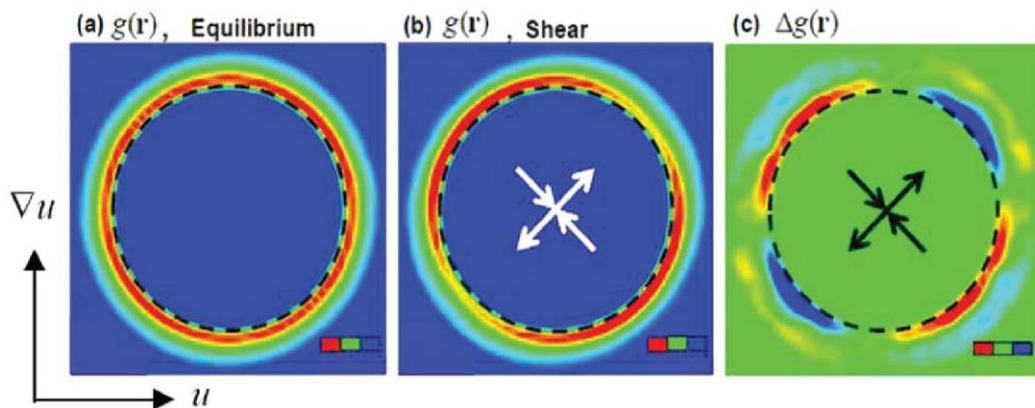


Figure 2.3 (a) The pair correlation function for a volume fraction of 45% in equilibrium, without shear flow. The color code indicates the value of the pair-correlation function (blue is a low value and red is a high value). (b) the same as in (a), but now for a shear rate corresponding to a Peclet number equal to $\tilde{\gamma} = 0.5$. The arrows indicate the compressional and extensional directions. (c) The difference between the pair correlation functions under shear in (b) and without shear in (a). The blue color code now corresponds to a negative value and the red color code corresponds to a positive value.

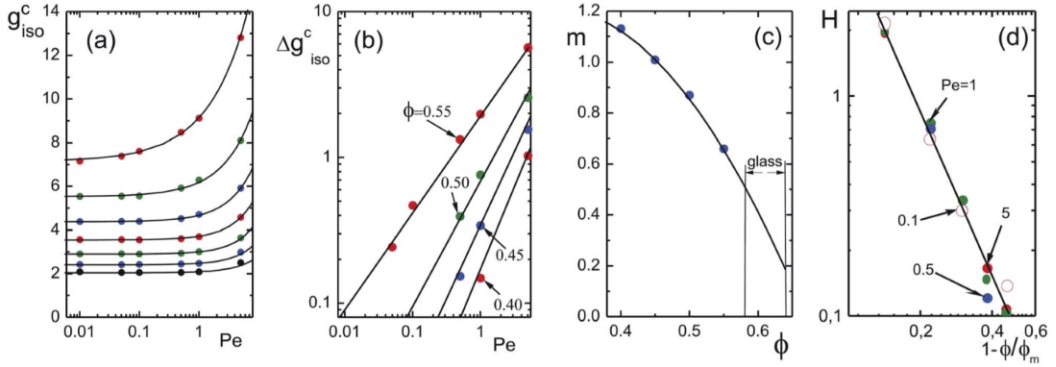


Figure 2.4 (a) The contact value g_{iso}^c of the isotropic part of the pair–correlation function as a function of the Peclet number for various volume fractions. The data points are BD–simulation results for $\phi = 0.25$ (the lower set of data points) up to $\phi = 0.55$ (the upper set of data points), increasing in steps of 0.05. (b) The difference Δg_{iso}^c between the isotropic contact values of the pair–correlation function of the sheared and unsheared equilibrium system as a function of the Peclet number for various volume fractions. The slope of the straight lines in this double–logarithmic plot is equal to the exponent m in Eq. (22). (c) The exponent m as a function of the volume fraction. The solid curve is the second order polynomial in Eq. (22). (d) The quantity $H \equiv \Delta g_{\text{iso}}^c / \tilde{\gamma}^m$ as a function of $1 - \phi / \phi_m$ on a double–logarithmic scale. The slope of the straight line is equal to the exponent $-s$ in Eq. (23). Some of the data points fall right on top of each other, so that they are not visible in this plot.

Concentration and shear-rate dependent contact values of the isotropic part of the pair-correlation function are shown in Figure 2.4a, where the data points are BD-simulation results for various volume fractions. As can be seen from Figure 2.4b, the shear-distorted part $\Delta g_{\text{iso}}^c = \Delta g_{\text{iso}}^c - \Delta g^{\text{eq},c}$ of the isotropic contact value of the pair-correlation function varies as $\sim \tilde{\gamma}^m$ for each volume fraction. The volume fraction dependence of m is shown in Figure 2.4c, where the solid line corresponds to,

$$m = 0.43 + 5.26\phi - 8.80\phi^2. \quad (22)$$

Note that, according to Eq. (3), (12) and (23), the osmotic pressure varies as $\sim \tilde{\gamma}^m$, where the Peclet number is to be interpreted as its absolute value, since reversal of the shear rate does not change the osmotic pressure. An approximate linear dependence of the shear-induced osmotic pressure on the applied shear rate is found experimentally in [26] for volume fractions ranging from 0.30 to 0.50 (see in particular Figure 2.3). The exponent m is indeed found in Figure. 2.4c to be close to unity within this range of volume fractions. As hydrodynamic interactions are neglected in BD simulations, it thus seems that the functional shear rate dependence is not too much affected by such hydrodynamic inter-colloidal interactions. It should be mentioned, however, that the Peclet numbers in [26] are extremely high,

so that the agreement between the results and those experiments may be fortuitous. A linear dependence of the osmotic pressure on the shear rate for concentrations below ϕ_g has also been proposed in [28]. Brownian dynamics simulations have been performed as in [27], likewise with the neglect of hydrodynamic interactions, where it is found that the pressure as obtained from the trace of the stress tensor corresponds to $m \approx 1.7$ for a volume fraction of 0.45 and for Peclet numbers ranging from 0.1 to 1. As the force in the advection–diffusion equation accounts for forces on the colloidal particles only, while the pressure obtained from the trace of the stress tensor includes in addition the forces on the solvent; the osmotic pressure discussed in the present paper is different from that in [27]. Gradients in the osmotic pressure as considered here lead to diffusive mass transport, while the pressure appearing in the Navier–Stokes equation in [27] leads to convective transport. This is the reason why a different exponent of 1.7 is reported in [27] as compared to the results.

As glass is “frozen–in liquid”, the microstructural order in the quiescent glass state is very similar to that in a fluid. This is most probably the reason why molecular dynamics simulations on hard–sphere systems find that the contact value of the pair–correlation function (without shear flow) changes smoothly from the fluid, to the meta–stable fluid region, to the glass state, on increasing the

concentration [45]. This also underlies the assumption in mode coupling theory that extrapolated structure factors from fluids to concentrations within the glass state can be used to assess the glassy dynamics. As yet, however, there are no rigorous arguments for smooth variations of structural variables from (meta-stable) fluids into the glassy state, for unsheared and for sheared systems. Here it is assumed that the same smooth variations as seen in simulations and often assumed for unsheared systems also hold true for sheared systems. As long as no crystallization occurs, the flowing branch of a glass most probably behaves very much like a concentrated flowing fluid. The concentration dependence of m within the fluid state is thus smoothly extrapolated into the glass state as shown in Figure 2.4c.

In Figure 2.4d the quantity $\mathbf{H} \equiv \Delta \mathbf{g}_{\text{iso}}^c / \tilde{\gamma}^m$ is seen to vary like $\sim (1 - \phi / \phi_m)^{-s}$, where $\phi_m = 0.64$ is the maximum random close packing volume fraction of spheres, and with, $s = 2.525$, independent of the shear rate. Furthermore, \mathbf{H} is found to be independent of the shear rate. These results imply that,

$$g_{\text{iso}}^c(\phi, \dot{\gamma}) = g^{\text{eq},c} + A \dot{\gamma}^m \left(1 - \frac{\phi}{\phi_m} \right)^{-s}, \quad (23)$$

is an accurate representation of the contact value of the isotropic part of the pair-correlation function. The value of the amplitude A is found to be equal to, $A = 0.0140$.

The solid lines in Figure 2.4a correspond to the representation (23), which is indeed seen to describe the BD-simulation data perfectly. The expression (23) for the pair-correlation function specifies the shear-rate and volume fraction dependencies of the transport coefficients in Eq. (14) and (15), which will be solved numerically for the Couette geometry in section 2.3.3.

2.3.2 Linear stability analysis and stability diagram

The linear stability analysis in previous work on the SCC–instability of colloids could only be done for zero wave vectors, since the non–local contribution, as quantified by the shear curvature viscosity, has not been included before. Without this contribution, the growth rate of variations/fluctuations of the flow velocity indefinitely increases with increasing wave vectors, which is unphysical. The non–local contribution renders variations/fluctuations of sufficiently large wave vectors stable, which is required to derive a physically meaningful dispersion relation.

Consider a flow in the x –direction with gradients in density and flow velocity only in the y –direction. Within the glass, the applied shear stress is supposed to be larger than the yield stress. Substitution of $\rho = \rho_0 + \delta\rho$ and $u = u_0 + \delta u$ into the advection–diffusion equation, where ρ_0 and $\dot{\gamma}_0$ are the constant initial density and shear rate respectively, and linearization with respect to the small perturbations $\delta\rho$ and δu gives,

$$\frac{\partial \delta\rho}{\partial t} = D_{\text{eff}} \frac{\partial^2 \delta\rho}{\partial y^2} + \xi \frac{\partial^3 \delta u}{\partial y^3}, \quad (24)$$

where D_{eff} and ξ are understood to be evaluated at the density ρ_0 and the shear rate $\dot{\gamma}_0$. The equation of motion for the flow velocity similarly gives,

$$0 = \frac{\partial \sigma}{\partial \dot{\gamma}_0} \frac{\partial^2 \delta u}{\partial y^2} + \frac{\partial \sigma}{\partial \rho_0} \frac{\partial \delta \rho}{\partial y} - \kappa \frac{\partial^4 u}{\partial y^4}, \quad (25)$$

where η and κ are evaluated at ρ_0 and $\dot{\gamma}_0$, and where,

$$\sigma = \dot{\gamma}_0 \eta(\rho_0, \dot{\gamma}_0), \quad \phi < \phi_g,$$

$$\sigma = \Sigma_{\text{yield}}(\rho_0) + \dot{\gamma}_0 \eta(\rho_0, \dot{\gamma}_0), \quad \phi \geq \phi_g,$$

are the shear-stress of the initially homogeneously sheared suspension, again at the density ρ_0 and the shear rate $\dot{\gamma}_0$. The time dependence of the perturbations will be exponential due to the linearization. The exponents for the density and flow velocity are the same, as the velocity is enslaved by the concentration. Hence, for sinusoidal spatial perturbations,

$$\delta \rho = \delta \rho_0 \exp(iky - \lambda(k)t),$$

$$\delta u = \delta u_0 \exp(iky - \lambda(k)t). \quad (26)$$

Substitution into Eq. (24) and (25) leads to the dispersion relationship,

$$\lambda(k) = k^2 \left[D_{\text{eff}} - \xi \frac{d\sigma}{d\rho} \left(\frac{d\sigma}{d\dot{\gamma}} + \kappa k^2 \right)^{-1} \right]. \quad (27)$$

According to Eq. (26), the initial density and flow profiles are unstable when $\lambda < 0$, that is, when,

$$D_{\text{eff}} \left(\frac{d\sigma}{d\dot{\gamma}} + \kappa k^2 \right) < \xi \frac{d\sigma}{d\rho} \rightarrow \text{unstable} \quad (28)$$

Since $\kappa > 0$, this result shows that perturbations corresponding to large spatial gradients, for which the corresponding wave vector k is

large, are stable. Only sufficiently smooth variations in the density and shear rate will be unstable, while rapidly varying variations remain stable. It thus follows from Eq. (28) that the system is unstable against arbitrarily smooth spatially varying perturbations (for which $k=0$), when the stability factor,

$$S \equiv \frac{\xi}{D_{\text{eff}}} \frac{d\sigma/d\rho}{d\sigma/d\dot{\gamma}}, \quad (29)$$

is larger than unity. This reproduces the SCC–stability criterion as derived similarly in [21–23]. The dispersion relationship (27) is most conveniently written in the dimensionless form as,

$$\Gamma = K^2 \left[1 - \frac{S}{1 + CK^2} \right],$$

where $\Gamma = \lambda(k)a^2/D_{\text{eff}}$ is the dimensionless (negative) growth rate, $K = ka$ is the dimensionless wave vector (with K the radius of the colloidal spheres), S is again the stability factor in Eq. (29), and $C = \kappa/(a^2 d\sigma/d\dot{\gamma})$. The quantity Γ/K^2 is plotted in Figure 2.5a as a function of K^2 for the typical values of $S = 2$ and $C = 200$ (solid curve) and $C = 400$ (dashed–dotted curve). Those wave vectors where $\Gamma < 0$ are unstable, while larger wave vectors corresponding to large spatial gradients remain stable. The fastest growing Fourier mode is the mode where Γ attains its minimum as shown in Figure 2.5b. The stabilization of Fourier modes with large wave vectors is solely due to the non–local stress contribution as characterized by the shear–curvature viscosity κ .

As can be seen, the larger the shear–curvature viscosity (to which C is proportional to), the smaller the wavevector range where the system is unstable. For $\kappa = 0$ the growth rate increases indefinitely like K^2 with the increasing wave vector. Such an arbitrarily fast growth of large spatial gradients is unphysical.

The critical wave vector k_c beyond which spatial variations are stable, for which $\lambda(k) = 0$, follows from Eq. (28) as,

$$k_c = \sqrt{\frac{d\sigma / d\dot{\gamma}}{\kappa}(S-1)}, \quad (S > 1) \quad (30)$$

while the fastest growing Fourier mode is the one with the wave vector k_m for which $d\lambda / dk = 0$, and hence,

$$k_m = \sqrt{\frac{d\sigma / d\dot{\gamma}}{\kappa}(\sqrt{S}-1)}, \quad (S > 1). \quad (31)$$

The above scenario for the initial banding kinetics is formally very similar to initial gas–liquid spinodal demixing kinetics as first described by Cahn and Hilliard [46, 47]. The equivalent of the shear–curvature viscosity is the square–gradient coefficient in the Cahn–Hilliard theory for spinodal decomposition. Similar to the higher order derivative in the expression for the stress tensor, the Cahn–Hilliard square–gradient coefficient multiplies a higher order spatial derivative in Fick's diffusion equation, which accounts for the increase in the free energy on formation of sharp concentration gradients. The shear–curvature contribution to the stress tensor was introduced in [6] to describe

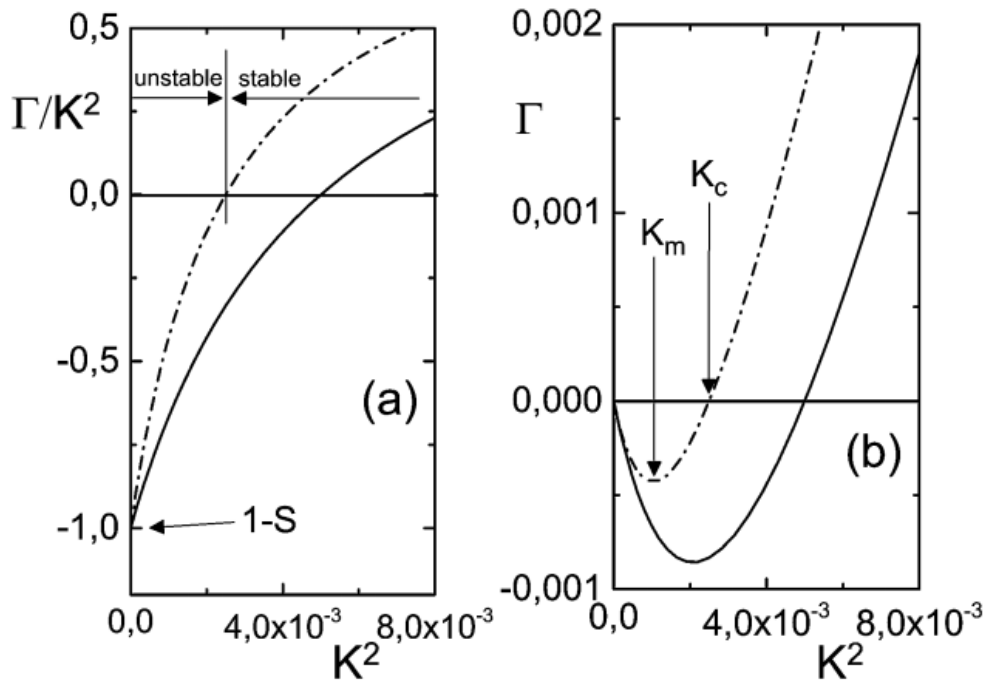


Figure 2.5 (a) The dimensionless quantity Γ/K^2 and (b) the dimensionless (negative) growth rate Γ as a function of the squared dimensionless wave vector $K = ka$. Here, $S = 2$ and $C = 200$ (solid curves) and $C = 400$ (dashed-dotted lines).

gradient–banding. The stabilization of fast growth of large spatial gradients through the shear curvature viscosity is a necessary feature for the numerical stability of algorithms to solve the above discussed equations of motion.

The stability criterion $S < 1$ in Eq. (29) together with the explicit forms of the transport coefficients discussed before allows construction of the stability diagram. This diagram marks the combinations of shear rates and concentrations where the system turns from being (meta–) stable to unstable. There is an essential difference between a system where the initial uniform volume fraction is smaller or larger than the glass–transition concentration ϕ_g . For $\phi < \phi_g$, it is given that $d\sigma/d\rho \sim \dot{\gamma}$, while for $\phi \geq \phi_g$, $d\sigma/d\rho \sim \text{constant}$ (for small Peclet numbers). This difference is due to the yield–stress contribution that is only present within the glass, and leads to a marked difference between the stability diagram for concentrations below and above the glass transition. As can be seen from Figure. 2.6a, for concentrations below the glass transition the uniform system is stable at least up to Peclet numbers of the order 1. Within the glass, in contrast, there is a large range of concentrations and relatively small shear rates where the uniform system is unstable. The thick solid line in Figure 2.6b marks the shear rates and concentrations where $S = 1$. This line marks the transition from the stable ($S < 1$) to the unstable state ($S > 1$) of a uniform system. The white and black data points in Figure 2.6b

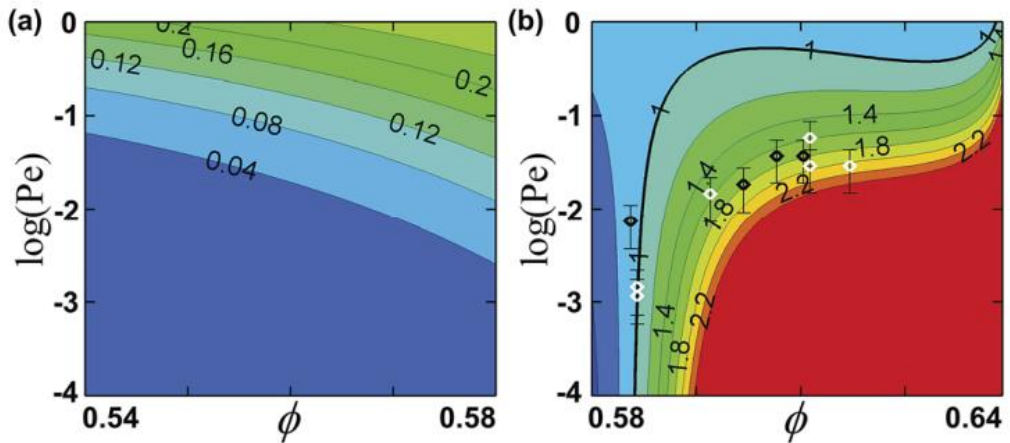


Figure 2.6 The stability diagrams in the shear-rate versus the concentration plane: (a) for $\phi < \phi_g$ and (b) for $\phi > \phi_g$. The thick line marks the transition from stable to unstable (where $S=1$). The iso- S lines are indicated by their corresponding values for S , whose curves are separated by a color code (red is a relatively high value of S and blue is a low value). The data points are experimental data for sterically stabilized PMMA particles: the white data points are for particles with a radius of 138 nm and the black data points for 150 nm, taken from [23].

are experimentally determined transition points for PMMA spheres, taken from [23]. In view of the neglect of hydrodynamic interactions, these data compare reasonably well with theory.

As will be seen in section 2.3.3, banding can also occur for concentrations very close to the glass transition concentration without a SCC–instability. The stability criterion (29) is thus a sufficient but not a necessary condition for a stationary banded flow.

In the notation of [23], n is the exponent appearing in the shear rate dependent stress for $\phi > \phi_g$. In our case $n=1/2$ (the exponent $-1/2$ in the expression for the shear rate dependent part of the viscosity, plus 1 as the viscosity is multiplied by the shear rate to obtain the stress). A similar value for $n=0.4-0.5$ is adopted in [23]. The value for m in Eq. (22) and (23), which describes the shear rate dependence of the osmotic pressure, is chosen in eqn (5) of [23] to be slightly smaller than n . The resulting value $m=0.4-0.5$ is similar to what we find in Figure 2.4c within the glass. The value of m , however, is found to be concentration dependent, varying from 0.5 for $\phi = \phi_g$ to 0.18 for $\phi = \phi_m$. The difference $m-n$ determines whether the $S=1$ stability curve in the stability diagram in Figure 2.6b slopes to the left or to the right: for $m-n > 0$ the $S=1$ curve has a negative slope, for $m-n < 0$ a positive slope. In the latter case the uniform glass becomes unstable on lowering the shear rate, which has been observed experimentally in [23]. Such a negative value of $m-n$ is also found in our analysis. The small

difference between m and n leads to the essentially shear rate independent location of the stability curve for the lower concentrations, as discussed in [23].

Note that Eq. (5) for the pair-correlation function is only accurate for Peclet numbers typically less than unity. The SCC instability within the glass state indeed occurs at Peclet numbers smaller than unity, as can be seen from Figure 2.6b. For fluids, however, the instability occurs at most at quite high Peclet numbers, as can be seen from Figure 2.6a. To analyze the SCC instability below the glass transition requires therefore a representation of the pair-correlation function that is also accurate at much higher Peclet numbers, which is beyond the scope of the present study.

2.3.3 Numerical results for concentration- and flow-profiles

It has not been possible in previous work on colloids to calculate the velocity and concentration profiles. There are no theoretical predictions yet concerning the velocity and concentration profiles resulting from the SCC-instability. An essential ingredient for the calculation of velocity and concentration profiles is the non-local contribution to the stress, as characterized by the shear-curvature viscosity, which stabilizes the system against arbitrary fast growth of variations/ fluctuations with large spatial gradients. Without this non-local contribution to the stress any numerical algorithm would be inherently unstable.

To solve the non-linear differential equations, a 2nd order central finite difference method is used to evaluate spatial derivatives, and a Newton-Rapson iteration is used to account for the non-linear term in the Navier-Stokes equation, while the time derivative is determined using the predictor-corrector iteration scheme based on the Crank-Nicolson method (Adams method) [48]. In the numerical calculation, a spatial discretization is used that sets the maximum value of the wave vector k_{\max} . When the number of grid points over an interval of length L is N_d , this maximum value of the wave vector is equal to $k_{\max} = N_d \pi / L$. In case k_{\max} is less than the critical wave vector k_c in Eq. (30), not all unstable Fourier modes are accounted for, and the numerical solutions are not realistic. A sufficiently fine grid must be chosen to assure that all unstable Fourier modes are accounted for. This is confirmed by

comparing numerical solutions with a different number of grid points. In this simulation, $N_d = 200$ and $d\tilde{t} = 2 \times 10^{-3}$, while $N_d = 400$ and $d\tilde{t} = 2 \times 10^{-4}$ are used to verify convergence.

The two coupled equations of motion for the concentration and flow velocity as discussed in section 2.2.3 will be solved numerically for a cylindrical Couette geometry (see Figure 2.7). Such a geometry features the inherent shear-gradients to induce the onset of the SCC-instability mechanism as explained in section 2.2. All variables are assumed to be fully-developed in the θ -direction (around the cylinder axis), and homogeneous in the z -direction (along the cylinder axis). The only relevant spatial coordinate is therefore the radial distance from the cylinder axis, which will be denoted by r . The simulation domain in this direction is set by the radii R_1 and R_2 of the inner and outer cylinder, respectively. The gap width $R_2 - R_1$ is chosen as $1000a$ (with a being the radius of the colloids), while $R_2 / R_1 = 0.98$. As will be seen later, the spatial varying volume fraction deviates at most of the order of 0.005 around the initial uniform volume fraction, so that banded flow profiles can be calculated from numerical solutions of equations of motion by taking m in Eq. (22) equal to its value corresponding to the initial volume fraction, independent of the position. To verify this procedure, the additional contributions due to the concentration dependence of m to the equations of motion can be estimated from the numerical solutions using a constant m .

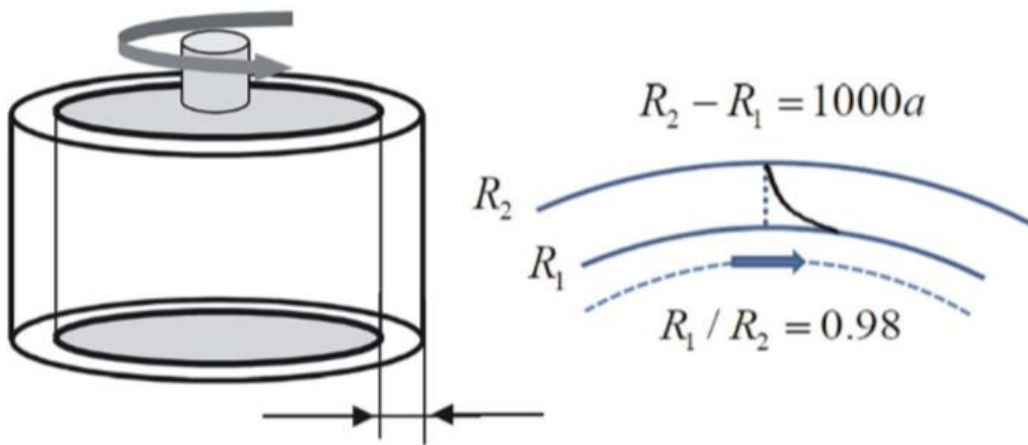


Figure 2.7 The cylindrical Couette geometry. The radius of the inner, rotation cylinder is R_1 , the outer radius of the stationary cylinder is R_2 . The gap width is chosen to be 1000 times the radius a of the spherical colloids, and $R_1 / R_2 = 0.98$.

The equation of motion for the concentration in terms of the radial cylindrical coordinate reads,

$$\frac{\partial \rho(r,t)}{\partial t} = \frac{1}{r} \frac{\partial}{\partial r} \left(r D_{\text{eff}} \frac{\partial \rho(r,t)}{\partial r} \right) + \frac{1}{r} \frac{\partial}{\partial r} \left(r \xi \frac{\partial \dot{\gamma}(r,t)}{\partial r} \right).$$

The stress is the sum of the yield-stress and a viscous-stress contribution,

$$\Sigma = \Sigma_{\text{yield}} + \Sigma_{\text{visc}},$$

where the yield stress is given in Eq. (23), while,

$$\Sigma_{\text{visc}} = \left(\eta - \kappa \frac{1}{r} \frac{\partial}{\partial r} \left\{ r \frac{\partial}{\partial r} \right\} \right) \dot{\gamma}(r,t).$$

The Navier-Stokes equation reads,

$$\frac{\partial}{\partial r} (r^2 \Sigma) = 0,$$

provided that the total local stress is larger than the yield stress. No-slip is assumed at both the walls of the inner and outer cylinder, that is, the suspension flow velocity is zero at the stationary outer wall where $r = R_2$, and equal to the non-zero wall velocity of the inner wall for $r = R_1$. The applied stress at the rotating inner cylinder will be fixed. There is no principle difference between the controlled stress and controlled shear rate experiments (contrary to gradient-banding in the absence of coupling to concentration, where banding does not occur under controlled stress conditions). The applied stress is hereafter specified by the dimensionless stress,

$$\tilde{\Sigma}(R_1) = \frac{\Sigma(r = R_1)}{k_B T / a^3}. \quad (32)$$

There are no mass fluxes through the walls of both cylinders: $j(R_1) = j(R_2) = 0$. Due to the inclusion of the shear–curvature contribution, a third set of boundary conditions is necessary. As the gap width is relatively small compared to the inner cylinder radius, so that variations of the shear rate are relatively small in the non–banded state, the third boundary condition is that the shear rates that are constant in the vicinity of the walls: $\partial \dot{\gamma} / \partial r = 0$ for both $r = R_1$ and $r = R_2$.

The remaining parameter that needs to be specified is the shear–curvature viscosity κ_0 . The interface thickness in a stationary shear–banded state is of the order $\sqrt{\kappa_0 / \eta_0}$, so that the dimensionless quantity,

$$\tilde{\Lambda} = \frac{1}{a} \sqrt{\frac{\kappa_0}{\eta_0}},$$

is a measure for the interface thickness in units of the radius a of the colloids. The interface thickness is probably much larger than the size of the colloids, so that $\tilde{\Lambda} = 100$ in the numerical analysis.

Stationary flow– and concentration–profiles for an initially homogeneous state are given in Figure 2.8. The initial overall concentration is 0.60, which is well within the glass. The dashed line in Figure 2.8a is the flow profile for the pure solvent, and the solid blue line corresponds to an initially stable suspension with an applied dimensionless stress at R_1 of $\tilde{\Sigma}(R_1) = 50$ (see Eq. (32)), while the red

curve corresponds to an initially unstable state with a dimensionless stress of 200. The velocities are normalized with respect to the velocity u_{wall} of the inner cylinder. The Newtonian velocity profile is essentially linear for the small gap width under consideration. The stable flow profile is somewhat curved, which is due to the shear-gradient induced mass flux. For the initially unstable state the final flow profile (the red curve in Figure 2.8a) exhibits a banded structure, where one band is non-flowing. The self-amplified mass flux leads to an increase of the concentration near the outer cylinder to an extent that the local yield stress becomes larger than the local applied stress, leading to an arrest of the local flow. The slight curvature within the flowing band near the non-flowing band is related to the width of the interface which is set equal to a tenth of the total gap width. In Figure 2.8b the difference between the velocity of a Newtonian fluid and the local velocity is plotted. The stationary concentration profiles are shown in Figure 2.8c. As can be seen, the variation of the concentration around the overall concentration is limited to about 0.01, which justifies using the value of the exponent m corresponding to the overall concentration. These small changes in the concentration are sufficient to induce a banded flow due to the strong concentration dependence of transport coefficients and viscometric functions.

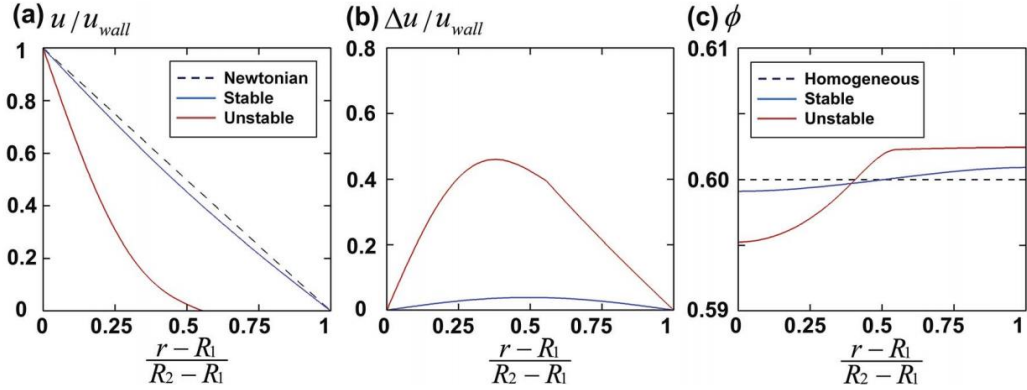


Figure 2.8 Stationary profiles for a volume fraction of 0.60, well within the glass. (a) Velocity profiles: the dashed blue curve is for a Newtonian fluid, the blue solid line is for a stable initial state where the applied dimensionless stress is equal to 200, and the red solid curve is for an unstable initial state with an applied stress equal to $\tilde{\Sigma}(R_1)=50$. The corresponding Peclet numbers are 1.0 and 0.0078, respectively. Velocities are normalized with respect to the velocity of u_{wall} of the rotating inner cylinder. (b) The difference of the flow velocity of a Newtonian fluid and the local velocity. (c) The position dependent volume fraction.

Banded flows can also occur for initially stable systems. For an overall concentration of 0.582 and an applied dimensionless stress of $\tilde{\Sigma}(R_1) = 14$, the stability parameter is always around 0.6. It is never larger than unity, neither in the initial state nor in the transient states. Nevertheless, a banded structure with very much the same features is found as the banded flow profile in the case of SCC-instability, as can be seen in Figure 2.9a (the red curve). The banded flow is now not due to the SCC-instability. The stability criterion discussed in Section 2.3.2 is thus a sufficient but not a necessary condition for banding. The reason for banding in this case is as follows. The local dimensionless stress at the outer cylinder is 13.446. This is just above the yield stress of 13.440 for the initial concentration. The shear-induced mass flux towards the outer cylinder, without self-amplification, is now sufficient to increase the local concentration to a value that leads to a local yield stress that is larger than the local stress, so that the local velocity vanishes, resulting in a banded flow profile. The slight increase in concentration at the outer cylinder is illustrated in Figure 2.9b (the red curve). For the small increase of the concentration that is necessary to lower the local stress at the outer cylinder below the yield stress, there is no need for self-amplifying the increase of concentration. For larger initial concentrations, the SCC-self-amplification mechanism is necessary to give rise to a sufficiently large increase of the local concentration such that the local yield stress becomes larger than the actual local stress at the outer

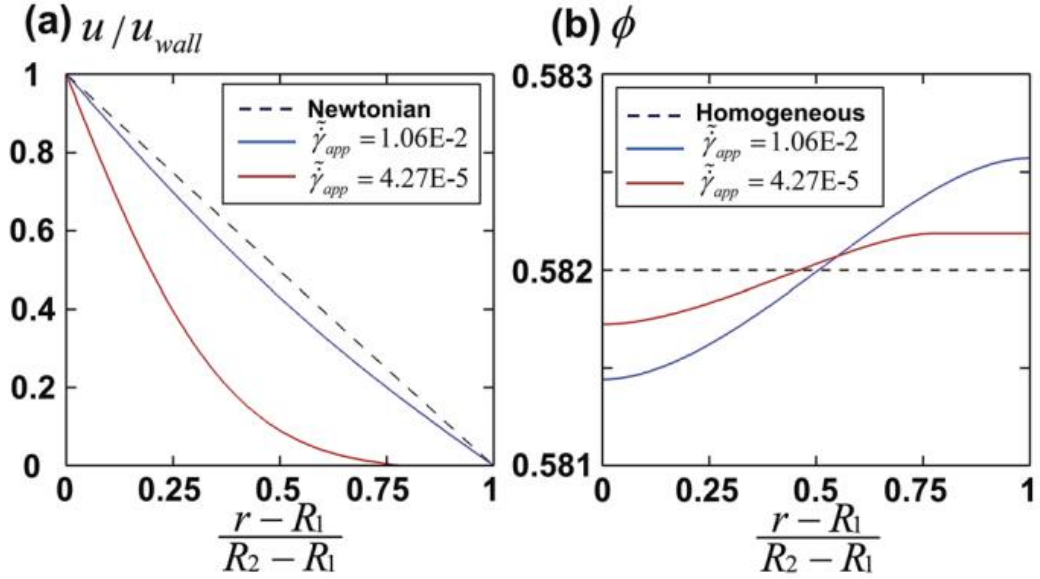


Figure 2.9 Stationary profiles starting from a stable state, for a concentration just above the glass transition, for an overall volume fraction of $\phi = 0.582$. (a) The velocity profile and (b) the volume fraction, for applied stresses of $\tilde{\Sigma}(R_1) = 14$ (the red curves) and 20 (the blue curves). The resulting apparent Peclet numbers $\tilde{\gamma}$ are indicated in the figure. The velocities are normalized by the velocity of the rotating inner cylinder u_{wall} . The black dashed line is the profile for a Newtonian fluid.

cylinder. The blue curves in Figure 2.9a and b are for a larger applied dimensionless stress of 20. For this relatively high applied stress, the local stress is always larger than the local yield stress so that there is no banding. As before, the curvature of the flow profile is now entirely due to the shear–curvature contribution to the stress.

It is, in principle, possible that in one part of the system, the concentration is above, and in the other part of the system, the concentration is below the glass–transition concentration. This only happens when the initial volume fraction is within 0.001 in the vicinity of the glass–transition concentration, and is therefore hardly of experimental relevance. A numerical solution for such cases would also require an entirely new computer algorithm in order to match the regions where the concentration is above and below the glass–transition concentration.

In analogy with thermodynamically driven phase transitions in the absence of flow, spinodals and binodals can be defined in the case of banding transitions [49, 50]. The spinodal is generally defined as the points where the system becomes unstable (this is the line where $S = 1$ in Figure 2.6b). As banding can also occur outside the unstable region where $S > 1$, as seen above, one might define the region where $S < 1$ but nevertheless banding occurs, as the meta–stable region, which is bounded by the binodal. Contrary to gradient–banding, however, the location of the binodal is not an intrinsic property of the system under consideration, but also depends on the shear–cell geometry. For

example, when the gap width of a Couette is increased, the natural spatial gradients in the shear rate are increased, which increases the shear–gradient induced mass flux, so that the banding of the SCC type for hard–sphere glasses occurs at lower concentrations. The binodal thus shifts to lower concentrations as the cell gap width is increased.

The temporal evolution of the flow and concentration profiles of the unstable system, for which stationary profiles are given in Figure 2.8, are shown in Figure 2.10. The initial condition here is a spatially constant concentration. The stability factor in the initial state is equal to 1.00077 and 1.00540, at $r = R_2$ and $r = R_1$, respectively. The typical wave length $2\pi/k_m$ of the (position dependent) most rapidly growing Fourier component is thus found from Eq. (31) to be of the order of the gap width. This explains the smooth growth of the profiles in Figure 2.10a and b. Similar smooth growth kinetics is found in the experiments in [23]. As the applied stress is fixed, the overall shear rate changes during band formation. This apparent Peclet number is plotted in Figure 2.10c. The temporal increase of the shear rate shows that the viscosity of the suspensions as a whole decrease during banding.

Under the initial conditions in the above examples, a spatially uniform density was chosen. Under a randomly chosen initial condition for the concentration (and hence the corresponding flow velocity), as a superposition of Fourier modes with wavelengths up to the gap width, leads to the same final state as for the uniform initial state. Higher order

Fourier modes decay fast, while the smooth variations slowly grow very much as for the uniform initial state. This is due to the value of the stability factor S , which is close to unity, so that according to the discussion in this section, only smooth spatial variations are unstable.

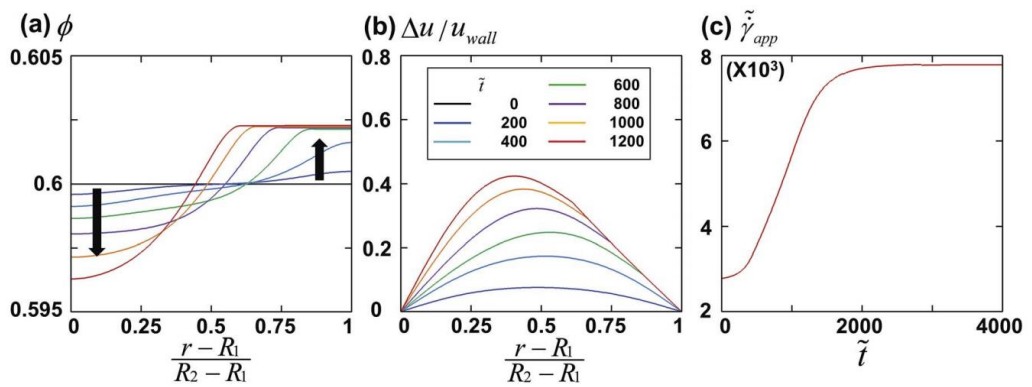


Figure 2.10 Temporal evolution of (a) the concentration profile, (b) of the velocity profile, and (c) of the apparent Peclet number. The various times $\tilde{t} = tD_0/a^2$ are indicated in (b). The overall volume fraction of 0.60, and the applied stress of $\tilde{\Sigma}(R_1) = 50$, of which the stationary profiles are given in Figure 2.8, (the red curves).

Chapter 3.

Non-local stresses in highly non-uniformly
flowing suspensions:

The shear-curvature viscosity

3.1 Introduction

Complex fluids can exhibit flow profiles in which there are unusually large spatial gradients in the local shear rate. For these highly non-uniformly flowing systems, there are contributions to the stress that arise from spatial variations of the shear rate, which are referred to as non-local stresses. Such large spatial gradients in the shear rate occur, for example, in micro-channel fluidics devices. Due to these large gradients, flow profiles in micro-channels cannot be described on the basis of the standard expression for the stress tensor. It is shown in [10] that non-local stresses are a necessary ingredient to describe the flow profiles of worm-like micellar systems in micro-channels with sufficiently large dimensions to describe the micellar solution as a continuum. Highly non-uniform flow profiles also occur when a fluid exhibits an instability that leads to gradient-banded flows. In the stationary state, two regions with spatially constant shear rates coexist. The shear rates within the bands are different for the two bands. The bands are connected by a sharp interface, where gradients in the shear rate are very large. There are two types of gradient-banding instabilities. A uniform flow profile is unstable when the stress decreases with increasing shear rate. In such cases, a transition occurs to a stable gradient-banded flow profile. Gradient-banding can also occur due to shear-gradient induced mass transport. Migration of

particles from regions of high shear rate to regions of low shear rate leads to concentration variations that in turn give rise to gradient-banded flow profiles. Two recent theoretical developments on shear-gradient induced diffusion of colloids and polymers can be found in [51] and [52], respectively. For both types of shear-banding scenarios, it is essential to include non-local stresses in the constitutive modeling of gradient-banding transitions, in order to account for the rapid spatial variations of the shear rate within the interface that connects the two bands.

The standard expression for the deviatoric part of the stress tensor for isothermal incompressible fluids reads

$$\boldsymbol{\Sigma} = -p\mathbf{I} + 2\eta\mathbf{D} \quad (33)$$

where p is the pressure, \mathbf{I} is the identity tensor, η is the viscosity, and $\mathbf{D} = (1/2)[\nabla\mathbf{v} + \nabla\mathbf{v}^T]$ (where “T” stands for transpose) is the symmetric part of the velocity gradient tensor $\nabla\mathbf{v}$ of the fluid velocity \mathbf{v} . This standard expression is obtained by formally expanding the stress tensor to first-order in gradients of the fluid velocity. There are two ways in which non-local stresses can be formulated. (i) A diffusive term can be added to the equation of motion for the stress tensor (see, for example, [53–56]), where the corresponding diffusion coefficient is referred to as the stress-diffusion coefficient. Such a constitutive approach has been used to determine the stress diffusion coefficient for

a micellar system from the kinetics of band formation [57]. This formulation of non-local stresses has also been applied to analyze the stability of the interface between gradient-bands [58], where an undulation instability of the interface can give rise to vorticity banding [59]. (ii) Another possibility to include non-local stresses is to simply extend the formal expansion of the stress tensor with respect to spatial gradients to include the next higher-order spatial derivative of the flow velocity, as compared to the leading order expansion in Eq. (33) [6, 56, 60]. For incompressible systems, this leads to,

$$\boldsymbol{\Sigma} = -p\mathbf{I} + 2[\eta - \kappa\nabla^2]\mathbf{D}, \quad (34)$$

where κ is referred to as the shear-curvature viscosity, as defined in previous chapter. The minus sign in the non-local stress contribution renders κ positive. This is the constitutive equation that has been successfully used in [10] to describe the flow profiles of worm-like micellar systems in micro-channels.

So far there are no (semi-)microscopic considerations to derive the constitutive relation in Eq. (34), which allow us to predict the magnitude of non-local stresses in bulk and, in particular, to predict or estimate the numerical value of the shear-curvature viscosity. It is the purpose of this paper to verify that the non-local stress contributions are of the form, as given in the constitutive equation (34), and to show that the shear-curvature viscosity κ is proportional to the shear viscosity η .

Brownian dynamics (BD) simulations are performed on a relatively simple system of spherical particles. To derive an approximate theoretical expression for the shear–curvature viscosity, an effective–medium argument is invoked in which each particle in the system is considered as being immersed in a continuum that represents the rest of the system. In preparation to apply this effective–medium theory, a system is solved, which is corresponding to hydrodynamic problem in section 3.2 of a single sphere in a continuum fluid, where the velocity of the fluid prior to insertion of the sphere is highly non–uniform. This analysis confirms the proposed structure for the constitutive equation in Eq. (34) and leads to an explicit expression for the shear–curvature viscosity. The effective medium approximation is further specified in section 3.3. The structure of the constitutive equation as well as the proportionality of the shear–curvature viscosity to the shear viscosity is verified by BD simulations of a relatively simple system of Brownian particles in section 3.4.

3.2 Non–local stresses for dilute suspensions:

the Einstein analog for the shear–curvature viscosity

Consider a sphere that is inserted in a fluid (hereafter referred to as the “solvent”) that undergoes, prior to insertion of the sphere, significant spatial variations over a length scale comparable to the size of the sphere. On insertion of the sphere, stresses will be generated that not only depend on the local shear rate of the fluid at the position of the sphere before insertion but also on the local spatial variations of the local shear rate. The latter contributions to the stress are the non–local stresses.

In order to evaluate the stress tensor for a system that consists of a strongly inhomogeneously flowing solvent in which an assembly of spheres is embedded, an expression for the divergence of the stress tensor is brought that is valid for inhomogeneous systems, as derived in [61],

$$\nabla \cdot \boldsymbol{\Sigma}(\mathbf{r}) = -\nabla \cdot [2\eta_0 \mathbf{D} - P_{ss} \hat{\mathbf{I}}] - \sum_{p=1}^N \left\langle \oint_{\partial V_p} dS' \delta(\mathbf{r} - \mathbf{r}') \mathbf{f}_p^h(\mathbf{r}') \right\rangle \quad (35)$$

where the shear stress $2\eta_0 \mathbf{D}$ (with η_0 as the shear viscosity of the solvent) and the pressure P_{ss} are due to solvent–solvent molecule interactions (hence the subscript “ss”). The last term is the contribution of the colloidal particles to the stress, where N is the number of

colloids under consideration, the integral ranges over the surface ∂V_p of the colloids, \mathbf{f}_p^h is the local force per unit area that the solvent exerts onto the surface elements of colloid p , and δ is the Dirac delta function. The brackets $\langle \dots \rangle$ denote averaging with respect to the position coordinates (and the orientations in the case of non-spherical particles) of the N colloids. This expression generalizes Batchelor's expression [62, 63] for the stress of homogeneously sheared systems to non-uniformly flowing systems. Batchelor's classic expression for the stress is obtained from Eq. (35) in the case of a constant shear rate and concentration. The interpretation of Eq. (35) for the stress tensor is rather straightforward: the integrals represent (minus) the force with which the surfaces of the colloids act onto the solvent, and the Dirac delta function counts only those colloids whose surfaces are located at position \mathbf{r} where the divergence of the stress is evaluated. This is what is expected for the force per unit volume (which is by definition the divergence of the stress tensor) produced by the colloids. In this section, an assembly of spheres embedded in a strongly inhomogeneously flowing solvent is considered, where the spheres do not mutually interact. For such very dilute suspensions, each sphere can be considered as being embedded in an otherwise unbounded solvent since the presence of the remaining spheres does not affect the flow for the sphere under consideration.

Note that when the solvent velocity varies over distances comparable to the size of the colloids, their Brownian motion results in quite large temporal fluctuations of the local stress. The brackets $\langle \dots \rangle$ in Eq. (35) represent the thermal average over these fluctuations and are thus only applicable for macroscopic time-dependent flows which vary sufficiently slow, as compared to the time required for the colloids to diffuse over distances comparable to their size.

In order to obtain an expression for the shear-curvature viscosity, the stress tensor needs to be expanded up to third order in the spatial gradient of the suspension flow velocity. Such a gradient expansion of the stress tensor with respect to spatial gradients is obtained by expanding the Dirac delta function in Eq. (35) according to

$$\delta(\mathbf{r}-\mathbf{r}') = \delta(\mathbf{r}-\mathbf{r}_p) + \sum_{n=1}^{\infty} \frac{(-1)^n}{n!} (\mathbf{r}'-\mathbf{r}_p)^n \odot \nabla^n \delta(\mathbf{r}-\mathbf{r}_p), \quad (36)$$

where the “ \odot ” denotes the contraction with respect to the polyadic products $(\mathbf{r}'-\mathbf{r}_p)^n = (\mathbf{r}'-\mathbf{r}_p)(\mathbf{r}'-\mathbf{r}_p)\cdots(\mathbf{r}'-\mathbf{r}_p)$ and $\nabla^n = \nabla\nabla\cdots\nabla$. Substitution into Eq. (35) leads to the following spatial-gradient expansion of the divergence of the stress tensor:

$$\begin{aligned} \nabla \cdot \boldsymbol{\Sigma}(\mathbf{r}) &= -\nabla \cdot [2\eta_0 \mathbf{D} - P_{ss} \hat{\mathbf{I}}] + \sum_{n=0}^{\infty} \nabla \cdot \boldsymbol{\Sigma}^{(n)}, \\ \nabla \cdot \boldsymbol{\Sigma}^{(n)} &= \frac{1}{n!} \nabla^n \odot \sum_{p=0}^N \left\langle \delta(\mathbf{r}-\mathbf{r}_p) \mathbf{T}_p^{(n)} \right\rangle, \end{aligned} \quad (37)$$

where the force moments $\mathbf{T}_p^{(n)}$ are defined as

$$\mathbf{T}_p^{(n)} \equiv (-1)^{n+1} \oint_{\partial V_p} dS (\mathbf{r}' - \mathbf{r}_p)^n \mathbf{f}_p^h(\mathbf{r}'). \quad (38)$$

The calculation of the surface force density on the sphere and the resulting force moments for the inhomogeneous flow under consideration is a technical mathematical problem. The resulting expressions for the force moments, up to contributions of fourth-order in spatial gradients of the flow velocity, are formulated in terms of the flow velocity \mathbf{u} of the solvent and the corresponding velocity gradient tensor $\mathbf{D} = (1/2)(\nabla\mathbf{u} + \nabla\mathbf{u}^T)$. Substitution of Eq. (36) to (38) into Eq. (35) leads to,

$$\begin{aligned} \nabla \cdot \boldsymbol{\Sigma}^{(0)}(\mathbf{r}) &= -\nabla \cdot [\rho k_B T \hat{\mathbf{I}}], \\ \nabla \cdot \boldsymbol{\Sigma}^{(1)}(\mathbf{r}) &= 5\eta_0 \nabla \cdot \left(1 + \frac{3}{50} a^2 \nabla^2 \right) [\phi(\mathbf{r}) \mathbf{D}(\mathbf{r})], \\ \nabla \cdot \boldsymbol{\Sigma}^{(2)}(\mathbf{r}) &= -\eta_0 a^2 \nabla \cdot \nabla^2 [\phi(\mathbf{r}) \mathbf{D}(\mathbf{r})], \\ \nabla \cdot \boldsymbol{\Sigma}^{(3)}(\mathbf{r}) &= \frac{1}{2} \eta_0 a^2 \nabla \cdot \nabla^2 [\phi(\mathbf{r}) \mathbf{D}(\mathbf{r})], \end{aligned} \quad (39)$$

where the volume fraction of colloids $\phi(\mathbf{r})$ is introduced,

$$\phi(\mathbf{r}) = \frac{4\pi}{3} a^3 \rho(\mathbf{r}) \quad (40)$$

The detail formulation procedure is in appendix A of [7], which applies ‘method of reflection’ [1] for the solvent velocity \mathbf{u} .

The leading gradient contributions to the divergence of the stress tensor are proportional to first-order gradients in the concentration and

to fourth-order in the flow velocity, in accordance with Eq. (34). Therefore only such leading order gradient contributions to the non-local stress will be kept, so that mixed terms like $\nabla\phi\cdot\nabla\mathbf{D}$ are neglected. Adding all terms in Eq. (39) for the various contributions to the body force originating from the colloids thus leads to

$$\begin{aligned}\boldsymbol{\Sigma}(\mathbf{r}) = & 2\eta_0\mathbf{D} - [\rho k_B T + P_{ss}] \hat{\mathbf{I}} \\ & + 5\eta_0\phi(\mathbf{r}) \left(1 - \frac{a^2}{25} \nabla^2 \right) \mathbf{D}(\mathbf{r}).\end{aligned}\quad (41)$$

It is thus finally found that the stress tensor takes the form (34) that was phenomenologically suggested in [6],

$$\boldsymbol{\Sigma} = -P\hat{\mathbf{I}} + 2[\eta - \kappa\nabla^2]\mathbf{D},\quad (42)$$

where the pressure P is equal to

$$P = P_{ss} + \rho k_B T,\quad (43)$$

the viscosity η is given by

$$\eta = \eta_0 \left(1 + \frac{5}{2} \phi \right),\quad (44)$$

and the shear-curvature viscosity is equal to

$$\kappa = \eta_0 \frac{a^2}{10} \phi\quad (45)$$

Equation (43) reproduces the ideal gas law for the osmotic pressure of dilute suspensions, Eq. (44) reproduces Einstein's expression for the

shear viscosity, and Eq. (45) is the corresponding analogous low-concentration expression for the shear-curvature viscosity.

Hence, on insertion of a sphere in a solvent with a constant shear rate (see Figure 3.1a), the additional stress caused by the presence of the sphere is equal to $\eta = 5\eta_0\phi\mathbf{D}$ [see Eqs. (42) and (44)]. On insertion of a sphere in a solvent with a curved flow profile [see Figure 3.1b], the curvature of the flow leads to yet another stress contribution equal to $-\eta_0(2a^2/5)\phi\nabla^2\mathbf{D}$ [see Eqs. (42) and (45)], which is the non-local contribution to the stress of dilute hard sphere suspension. In conclusion, the non-local contribution can be originated from the distorted stresslet distribution on the surface of particle.

However, still, this this formulation lacks the contribution from the interaction between the particles, which stands for the true origin of non-local stress. Though it seems that adding force density due to particle interaction into Eq. (35) would lead to such non-local stress, it is not feasible because of the difficulties in considering the non-uniform flow field within the interaction range of the particles.

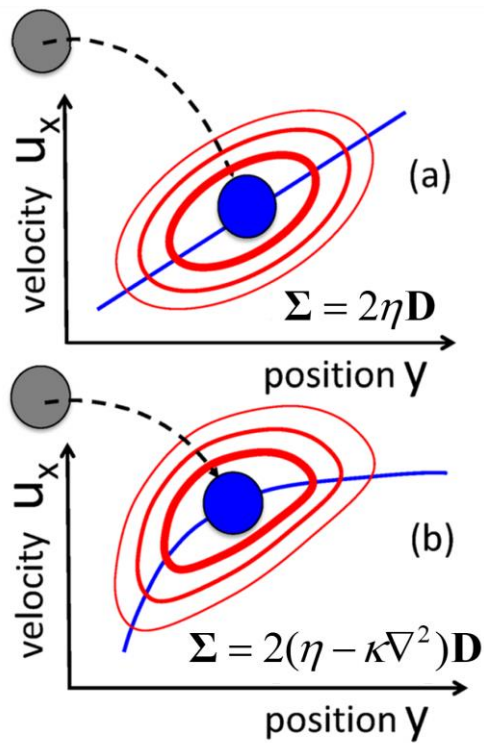


Figure 3.1 Insertion of a sphere into a flowing solvent (the gray sphere before insertion and the blue sphere after immersion). This sketch pictures the solvent's flow velocity in the x -direction (the blue solid lines) that varies in the y -direction for (a) a solvent flow velocity with a constant shear rate and (b) for a spatially varying shear rate. The red lines schematically depict equidistant stress areas corresponding to the flow fields generated after insertion of the sphere. The corresponding expressions for the suspension stress tensor are indicated in the figures. The additional curved flow in (b) gives rise to an additional stress equal to $-2\kappa\nabla^2\mathbf{D}$

3.3 An effective medium approximation for the shear–curvature viscosity

Within an effective–medium approach, the inhomogeneously flowing solvent in the considerations in section 3.2 is replaced by the suspension of colloidal spheres which are identical to the sphere that is inserted. The suspension is thus considered as an effective medium that behaves like a solvent for the inserted sphere. The viscosity η_0 of the solvent in Eq. (45) is thus simply replaced by the shear viscosity η of the suspension at the given volume fraction ϕ and shear rate $\dot{\gamma}$. According to Eq. (45), $\kappa \sim \eta_0$, that is, the contribution to the shear–curvature viscosity per colloidal sphere is linearly related to the shear viscosity. Since in concentrated suspensions each sphere on average contributes equally to the stress (corresponding to the particle–surface integrals in Eq. (35)), the effective–medium approach thus states that the additive contribution of each sphere to the shear–curvature viscosity is proportional to the suspension viscosity. This leads to the following effective–medium approximation for the shear–curvature viscosity:

$$\kappa(\phi, \dot{\gamma}) = \eta(\phi, \dot{\gamma}) \frac{a^2}{10} \phi = \frac{4\pi}{30} \eta(\phi, \dot{\gamma}) \frac{a^5}{10} \rho \quad (46)$$

where the volume fraction, the number concentration ρ , and the shear rate are understood to be evaluated at position \mathbf{r} . This expression for

the shear curvature viscosity quantifies the non-local stress due to spatial variations of the shear rate and the concentration and will be compared to simulations in section 3.4. Note that the above effective medium approximation predicts a shear rate dependence of the shear curvature viscosity that is similar to that of the shear viscosity.

It is important to realize that the radius a in the effective medium approach differs from the hard core radius of the sphere. A sphere that is inserted in a suspension does not behave like a sphere with stick boundary conditions precisely at the geometrical boundary of that sphere. The volume fraction in the first equation in (46) is therefore not the volume fraction that corresponds to the hard-core radius of the sphere. In a comparison with simulations in section 3.4, it is therefore necessary to make the distinction between a in Eq. (46) and the hard-core radius of the spheres. Hereafter a is referred as the effective radius, which is the radius of a sphere that leads to an increase in the stress on insertion into the suspension when the suspension for that sphere behaves like a solvent with stick boundary conditions. The effective radius will be larger, but of the same order of magnitude, as the hard-core radius, which will be discussed in more detail later.

The effective medium result (46) for the shear curvature viscosity will be validated against Brownian dynamics simulations in section 3.4.

3.4 Brownian dynamics simulation

The effective-medium approach discussed above is an approximation, the accuracy of which will be tested against Brownian dynamics (BD) simulations. In principle, one may perform simulations where the interactions between the colloids and their coupling to the stress lead to gradient banding [64–66]. Since non-local stresses are only significant within the sharp interface that separates the two shear-bands and only a small fraction of the colloids reside within the interface, such simulations would suffer from bad statistics. Therefore, the simulation between parallel plates is chosen, which may be considered as a two-dimensional analog of the type of flow encountered in micro-fluidics devices. Essentially all the colloidal spheres now experience a highly non-linear flow. In order to probe the non-local stress with sufficient statistics for a quantitative comparison to the effective-medium prediction, a large number of particles must be simulated. Including full hydrodynamic interactions between the colloidal particles would therefore require unrealistically long computation times. The simulated fluid of Brownian spheres plays the role of the effective medium into which the sphere is immersed. On a continuum level, this Brownian fluid acts as a hydrodynamic medium. Therefore, as a proof of principle, the particle simulation is conducted with Brownian spheres that are subject to a spatially sinusoidally varying driving body force in the direction parallel

to the confining plates in the absence of a solvent. The imposed body force is nothing but a means to induce a non-linear flow profile, which does not affect the measured shear-stress directly, but only indirectly through inter-particle interactions. Thus, the fundamental evolution equation for the BD-simulation is given as following, which is same with BD simulation in chapter 2, subsection 2.2.2, except for the extra sinusoidal force field.

$$d\mathbf{r} = \frac{1}{\xi} (\mathbf{F}_i^{imp} + \mathbf{F}_i^p) dt + \sqrt{2D_0 dt} \mathbf{W}_i, \quad (47)$$

where ξ is the friction coefficient and D_0 is the diffusion coefficient that sets the time scale of Brownian motion, and \mathbf{W}_i is a Gaussian variable with average zero and variance unity. Furthermore, \mathbf{F}_i^{imp} is the above mentioned imposed force on particle i in the x -direction with its gradient in the y -direction. The imposed force gives rise to an imposed velocity \mathbf{v}_i^{imp} of particle i equal to

$$\mathbf{v}_i^{imp} = \left[\bar{\gamma} y_i + \frac{\dot{G}_0}{k} \sin ky_i \right] \hat{\mathbf{e}}_x, \quad (48)$$

with y_i as the y -component of the position coordinate \mathbf{r}_i of particle i and $\hat{\mathbf{e}}_x$ as the unit vector in the x -direction. The first term corresponds to a simple shear velocity with shear rate $\bar{\gamma}$, and the second term is a superimposed sinusoidally varying velocity with wave

number k and amplitude \dot{G}_0/k . \mathbf{F}_i^p is the force on particle i due to direct interactions with other particles,

$$\mathbf{F}_i^p = -\sum_{\substack{j=1 \\ j \neq i}}^N \nabla_i V(|\mathbf{r}_i - \mathbf{r}_j|) \quad (49)$$

with $V(r)$ being the inter-colloidal pair interaction potential. For the pair-interaction potential, a hard-core potential corresponding to a sphere with radius R is chosen, augmented with a standard DLVO potential as,

$$V = V^{\text{overlap}} + V^{\text{el}} + V^{\text{vdW}}$$

where

$$V^{\text{overlap}} = \begin{cases} 0 & r \geq 2R \\ \infty & r < 2R \end{cases}$$

$$V^{\text{vdW}} = -\frac{A_H}{12} \left[\frac{4R^2}{r^2 - 4R^2} + \frac{4R^2}{r^2} + 2 \ln \left(\frac{r^2 - 4R^2}{r^2} \right) \right],$$

$$V^{\text{el}} = k_B T \exp(-\kappa_D(r - 2R))$$

where A_H is the Hamaker constant, κ_D is the Debye length, and

$$E = \frac{32\pi R\epsilon}{z^2 e^2} \tanh^2 \left(\frac{ze\psi_0}{4k_B T} \right)$$

is the electrostatic potential energy in units of $k_B T$ at contact of two sphere. The interaction parameters are chosen as $A_H = 0.77k_B T$, $\kappa_D^{-1} = 0.1R$, and $E = 50$ (corresponding to $1\mu\text{m}$ spheres with a surface potential of 7 mV in monovalent ionic aqueous solution).

The simple linear shear flow is maintained by Lees–Edwards boundary conditions, while the wave number $k = 2n\pi / L$ with $n = 1, 2, \dots$ and L is the height of the simulation box.

To calculate ensemble averaged quantities at a given position \mathbf{r} , the simulation domain is divided into 200 slabs that are stacked along the gradient direction, spanning the flow vorticity plane. The ensemble averaged macroscopic velocity profiles are thus obtained from

$$v(y) = \frac{1}{N(y)} \sum_{y_i \in \text{slab}(y)} v^p(y_i) \quad (50)$$

where the summation ranges over particles which reside within the slab with its position at y_i and with a velocity $v^p(y_i)$ and where $N(y)$ is the number of spheres within the same slab. The local macroscopic stress $\sigma(y)$ is determined in the same way, where stresses arising from interactions with particles outside the slab are accounted for the averaging procedure, where inter–particle forces of particles whose line segment intersects with the slab under consideration are included in the stress computation, and account for contributions to the stress originating from spatial inhomogeneities [67]. The BD simulations are also used to obtain the shear rate dependence of the viscosity, for which $\dot{G}_0 = 0$. All simulations start from equilibrated states, which are achieved from simulations without flow over an extended period of time (more

than 20 times R^2/D_0). The stationary state under flow conditions is subsequently reached after an additional simulation under flow conditions over a time period of at least $100 \times R^2/D_0$ for homogeneous shear flow and $1000 \times R^2/D_0$ for inhomogeneous shear flow. Flow and stress profiles are obtained once the stationary state is attained in the way described above. The dimensionless time interval $dt^* = (D_0/R^2)dt$ is chosen as 5×10^{-5} , which is verified to be sufficiently small. The number of BD simulation time steps for an inhomogeneous flow is at least equal to 2×10^7 . The system consists of 16,000 spheres, dispersed within a rectangular box. The length of the box along the shear gradient direction is twice larger than that in the other two directions, in order to achieve a sufficiently finely divided set of values of the wave numbers $k = 2n\pi/L$. The volume fraction corresponding to the hard-core radius R of the spheres is 0.30, so that the size of the cube along the gradient direction is about 100 times the particle radius. The simulation box size is much larger than the distance over which particles are correlated. True bulk properties are therefore probed, assuring that the shear-curvature viscosity as obtained from the simulations is a true material function.

3.5 Results and discussion

In this section, the results of BD simulations is presented and it is compared with the effective-medium approximation presented in section 3.3. All results will be presented in the dimensionless form in identical way with chapter 2, except for characteristic stress. Here, stresses are non-dimensionalized by $k_B T / 6\pi R^3$, rather than $k_B T / R^3$ for convenience.

Hence, the expression for the shear stress σ , that is, the xy -component of the stress tensor in Eq. (34) is

$$\sigma^* = \eta^* \left(1 - \frac{\kappa^*}{\eta^*} \phi \nabla^{*2} \right) \dot{\gamma}^* \quad (51)$$

where the dimensionless gradient operator ∇^* is equal to $R\nabla$ and the “relative viscosity” is equal to

$$\eta^* = \eta \frac{6\pi R D_0}{k_B T} \quad (52)$$

Note that for a Brownian particle in a solvent, $\eta^* = \eta / \eta_0$, with η_0 being the shear viscosity of the solvent, while the dimensionless shear-curvature viscosity is defined as

$$\kappa^* = \kappa \frac{\eta^*}{R^2 \tilde{\phi} \eta} = \kappa \frac{6\pi D_0}{k_B T R \tilde{\phi}}. \quad (53)$$

where $\tilde{\phi} = 4\pi R^3 \rho / 3$ is the hard-core volume fraction. Note that this volume fraction differs from the volume fraction ϕ in sections 3.2 – 3.4, which is based on the effective radius.

As a first step, the viscosity of a homogeneously sheared system (for which $\dot{G}_0 = 0$) is simulated as a function of the shear rate, for a given volume fraction of $\tilde{\phi} = 0.3$. The relative viscosity as a function of the Peclet number $\bar{\gamma}$ is given in Figure 3.2. The black solid line is a fit of the blue simulation data points to the empirical Carreau–Yasuda viscosity equation, which has been shown before to accurately describe viscosity data [68],

$$\eta^*(\dot{\gamma}) = \eta_\infty + \frac{\eta_q - \eta_\infty}{[1 + (\lambda\dot{\gamma})^2]^m} \quad (54)$$

where η_q is the zero-shear viscosity, η_∞ is the high-shear viscosity, λ is a relaxation time, and m is a power-law index. The Carreau–Yasuda fit will be used later in order to analyze the numerical results for inhomogeneously sheared systems.

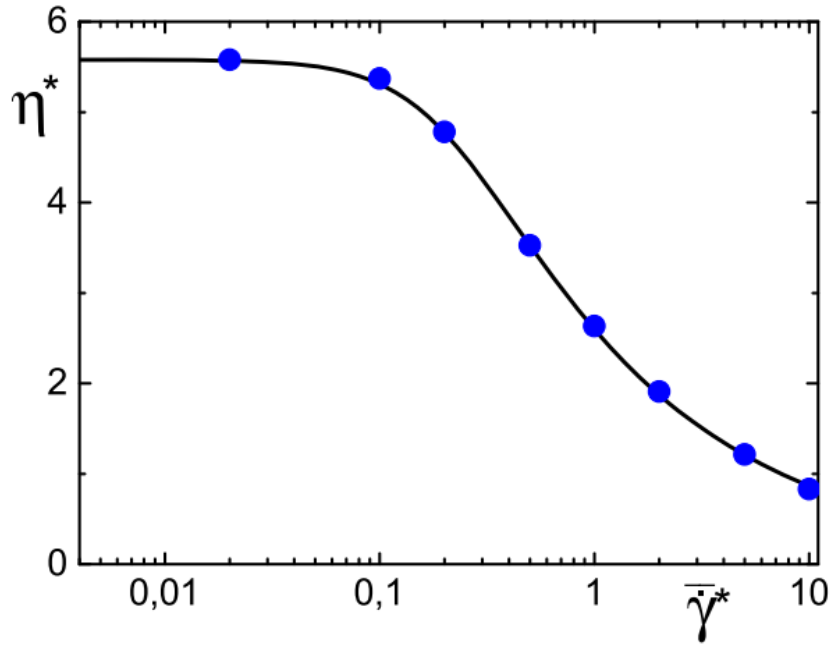


Figure 3.2 The relative viscosity of a homogeneously sheared system with a volume fraction of $\tilde{\phi} = 0.3$ as a function of the Peclet number $\bar{\gamma}$. Blue data points are simulation results, and the black solid line is a fit to the empirical Carreau–Yasuda function (54). The values of the fitting parameters are $\eta_q = 5.6$, $\eta_\infty = 0$, $\lambda = 4.87$, and $m = 0.24$.

Since the imposed velocity in Eq. (48) for the inhomogeneously sheared systems is sinusoidal, the corresponding resulting particle velocities will be similarly sinusoidal, with an amplitude of approximately \dot{G}_0/k . The local shear rate is, therefore, equal to $\bar{\dot{\gamma}} + \dot{G}_0 \cos ky$. In the simulation, \dot{G}_0 is a constant, in order to fix the values of local shear rates for each different wave number. The amplitude of the sinusoidal flow-velocity perturbation is chosen to be small as compared to the linear flow velocity corresponding to the shear rate $\bar{\dot{\gamma}}$. The reason for this is to clearly separate the local and non-local stresses. In case the amplitude of the sinusoidal flow velocity would be relatively large, there would be a significant sinusoidal variation of the stress $\bar{\dot{\gamma}}$ due to the spatial variation of the shear viscosity itself on top of the non-local stress. The lower limit of the amplitude \dot{G}_0 to obtain accurate results is about $\dot{G}_0 = D_0 / (10R^2)$. The local shear-rate amplitude is not exactly equal to \dot{G}_0 since direct inter-colloidal interactions change the flow profile. The local velocity is therefore written as

$$v(y) = \bar{\dot{\gamma}} y + \frac{\dot{G}}{k} \sin ky, \quad (55)$$

where the amplitude \dot{G}/k is determined from a fit of the simulated flow profile. The local shear rate is obtained by the differentiation of Eq. (55),

$$\dot{\gamma}(y) = \bar{\dot{\gamma}} + \dot{G} \cos ky, \quad (56)$$

or in dimensionless variables

$$\dot{\gamma}^*(y^*) = \bar{\dot{\gamma}}^* + \dot{G}^* \cos k^* y^*, \quad (57)$$

where dimensionless quantities are introduced as before. An example of a velocity and shear-rate profile is shown in Figure 3.3 for a Peclet number $\bar{\dot{\gamma}}^* = 0.5$ and a wave number of $k = 4\pi / L$. The velocity profile is plotted in Figure 3.3a, from which the amplitude $V = \dot{G}^* / k$ is determined by a fit to Eq. (55), which is indicated by the red solid curve. The corresponding shear rate profile as obtained from numerical differentiation of the simulation data is plotted in Figure 3.3b.

Substitution of Eq. (57) for the inhomogeneous shear rate into Eq. (51) for the stress leads to

$$\sigma^*(y^*) = \eta^*(\dot{\gamma}^*(y^*)) \left[\bar{\dot{\gamma}}^* + \dot{G}^* \left(1 + \frac{\kappa^*}{\eta^*} \tilde{\phi} k^{*2} \right) \cos k^* y^* \right], \quad (58)$$

where the relative shear viscosity is evaluated at the local shear rate given in Eq. (57). Examples of inhomogeneous shear stress profiles are given in Figure 3.4a for an average shear rate of $\bar{\dot{\gamma}}^* = 0.5$ and for $n = 1, 2, 3, 4$ (the black, green, blue, and red data points and fits, respectively).

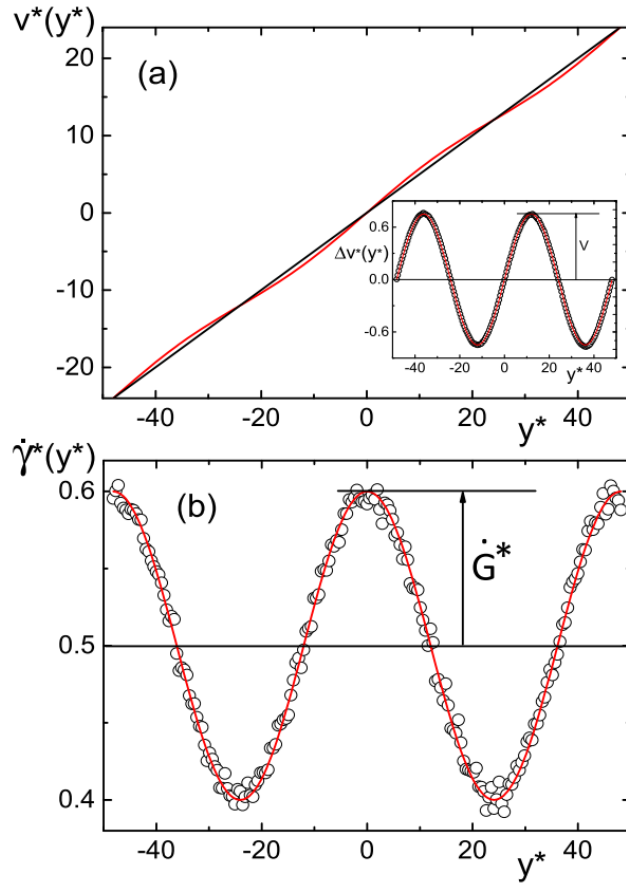


Figure 3.3 (a) The velocity profile obtained from a simulation with $\bar{\gamma}^* = 0.5$ and with a wave number equal to $k = 4\pi / L$. The black solid line corresponds to a linear flow with a constant shear rate $\bar{\gamma}^* = 0.5$, and the red line is a sinusoidal fit to the actual velocity profile. The inset shows the corresponding plot for $\Delta v^* = v^* - \bar{\gamma}^* y^*$, where the open data points are simulation data. (b) The shear rate profile obtained from numerical differentiation of the data points shown in the inset in (a). The red solid line is obtained from the fitted curve in (a), which corresponds to Eq. (57).

The solid lines in Figure 3.4a are the result of a global least square fitting of all the stress profiles simultaneously. One fit parameter is the dimensionless parameter,

$$\Lambda_0 \equiv \frac{\kappa^*}{\phi \eta^*} = \frac{\kappa}{R^2 \phi \eta} \quad (59)$$

According to the effective-medium approximation (46), this dimensionless parameter should be equal to

$$\Lambda_0 = \frac{1}{10} \left(\frac{a}{R} \right)^5. \quad (60)$$

As before, a is the effective radius, while R is the hard-core radius of the spheres. The effective-medium approximation thus predicts that Λ_0 is independent of the applied mean shear rate $\bar{\gamma}$. Two more fitting parameters are introduced, which are necessary to correct for the errors involved in the independently obtained simulated viscosity data, for which the Carreau-Yasuda fit in Eq. (54) is used. Thus, following square is minimized,

$$\varepsilon(\Lambda_0, C_1, C_2 | \bar{\gamma}^*) = \sum_{k^*} \sum_j [\sigma^{*,\text{model}}(y_j^* | \Lambda_0, C_1, C_2 | \bar{\gamma}^*, k^*) - \sigma^{*,\text{sim}}(y_j^* | \bar{\gamma}^*, k^*)] \quad (61)$$

where the first sum ranges over all the different wave numbers (corresponding to all the stress profiles shown in Figure 3.4a and the

second sum ranges over all positions where the stress is evaluated. Here, $\sigma^{*,\text{sim}}(y_j^* | \bar{\gamma}^*, k^*)$ is the simulated stress, and

$$\sigma^{*,\text{model}}(y_j^* | \Lambda_0, C_1, C_2 | \bar{\gamma}^*, k^*) = \eta^*(\bar{\gamma}^*(y_j^*)) [C_1 \bar{\gamma}^* + C_2 \dot{G}^* (1 + \tilde{\phi} k^{*2} \Lambda_0) \cos k^* y_j^*] \quad (62)$$

corresponds to the stress in Eq. (58), except for the two additional fitting parameters $C_{1,2}$ which account for the inaccuracy of the viscosity BD simulation results. The fitting values of these two parameters should be close to unity. A fit for each separate wave vector (using the values for $C_{1,2}$, as found in the global fits) gives numerical values for Λ_0 in Eq. (62), where the linear dependence on k^{*2} in Eq. (62) at the constant of cosine term is the prediction from the theory.

Figure 3.4c shows the global fitting result for one of the stress profiles that is also given in Figure 3.4a (with $n=4$). The inset shows the difference between the fitting results including the non-local stress and that without the contribution from the non-local stress. The comparison between these fits shows that non-local stresses are essential to describe the simulated stress profiles.

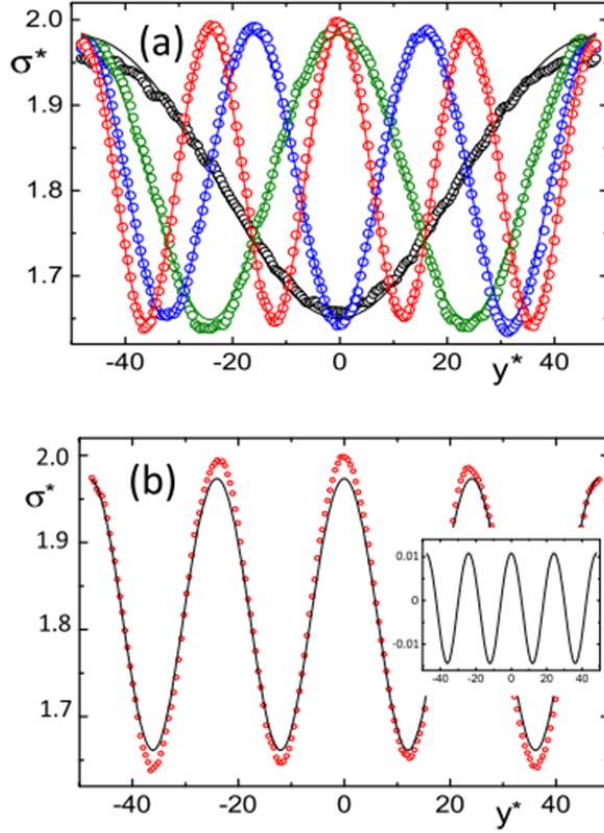


Figure 3.4 (a) The local shear stress σ^* under inhomogeneous shear flow for an average shear rate $\bar{\dot{\gamma}}^* = 0.5$ and for four different wave numbers $k = 2n\pi/L$ with $n = 1, 2, 3, 4$, corresponding to the black, green, blue, and red simulation data points, respectively. The solid lines are global fits for all wave vectors simultaneously to Eq. (62). (b) The simulated stress profile as in (a) for $n = 4$, where now the solid line is the best global fit result with the neglect of non-local stress contributions. The inset shows the difference between the fitting result for the stress profile with and without contributions from the non-local stress.

Results for the fitting parameters for three different values of the Peclet number $\bar{\gamma}^*$ are given in Figure 3.5a. As can be seen from this figure, the values of $C_{1,2}$ are quite close to unity, as they should, while the value of $\Lambda_0 = 3.8 \pm 0.5$ is constant and independent of $\bar{\gamma}^*$ to within simulation errors, as predicted by the effective-medium approximation (see Eq. (60)). According to Eq. (60), the numerical value of Λ_0 found in Figure 3.5a corresponds to $(a/R)^5 = 38 \pm 5$, and hence $a/R = 2.07 \pm 0.06$. That is, the effective radius of a sphere in the simulated system in the absence of hydrodynamic interactions is about two times larger than its hard-core radius. This is of the same order as the distance from a sphere over which the hydrodynamic behavior of a suspension sets in as found in simulations of Brownian hard-spheres without hydrodynamic interactions in 2D [69]. The relative viscosity $\eta_\kappa^* \equiv 10\kappa / (a^2\phi)$ that follows from the effective-medium prediction in Eq. (46) with the numerical value of $\Lambda_0 = 3.8$ and $a/R = 2.07$ is plotted in Figure 3.5b. This plot confirms the proportionality $\kappa \sim \eta$, as predicted by the effective-medium expression for κ in Eq. (46), within a shear-rate range where the viscosity significantly shear-thins.

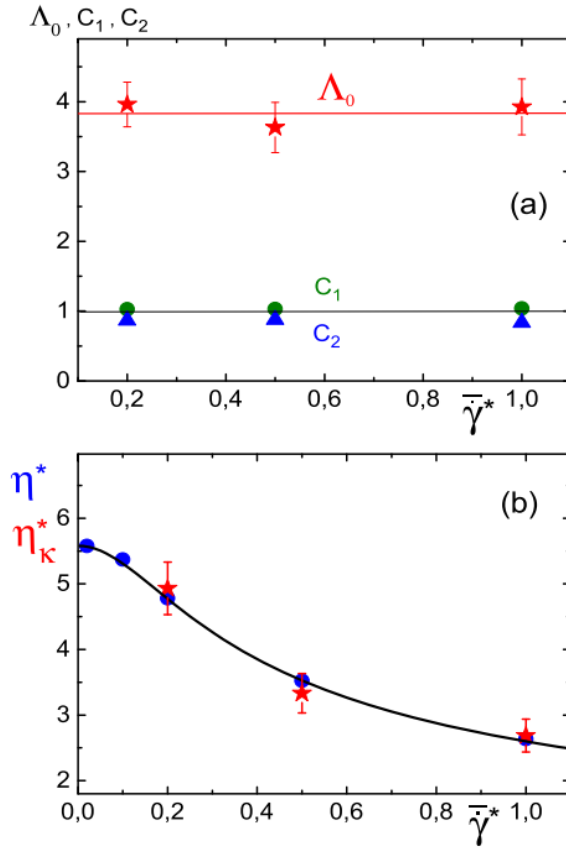


Figure 3.5 (a) Results of the least-square fits for Λ_0 , C_1 , and C_2 (the red stars, green circles, and blue triangles, respectively) for three values of the Peclet number $\bar{\gamma}^* = 0.2, 0.5$, and 1.0 . The horizontal red line is the weighted average of the three data points for Λ_0 . (b) The relative viscosity (in blue) as compared to the relative viscosity η_{κ}^* as obtained from the numerical values for $\Lambda_0 = 3.8$ and $a/R = 2.07$ (in red) according to the effective-medium approximation in Eq. (46).

Chapter 4.

Concluding remark

In this thesis, the mass flux and the extra stress due to non-uniform flow field is investigated. In chapter 2, physical origin of shear rate gradient induced mass flux is elucidated. It is found that the ‘spatial gradient’ of shear distorted pair correlation function gives rise to the gradient of ‘generalized’ particle pressure, which push the particles from high shear rate region to low shear rate region. The values of shear-distortion of pair correlation function under various flow conditions are obtained from Brownian dynamics simulation, so that the mass flux coefficient are given as a function of shear rate and concentration. And then, the shear banding dynamics due to the coupling between the mass flux and momentum is analyzed by numerical simulation using finite difference scheme.

In chapter 3, the constitutive relation of particulate suspension including the non-local contribution is derived first for dilute hard sphere suspension, applying non-uniform flow condition and spatial expansion to the most general expression of particle stress tensor. The result shows that the shear curvature viscosity is proportional to the shear viscosity, which can be regarded as extended Einstein equation. Brownian dynamics simulation with sinusoidally varying velocity field is performed to check the validity of such proportionality in more complicated system. In the Brownian dynamics, regression of local shear stress profiles with respect to the constitutive model with non-local

stress gives the shear curvature viscosity as a function of shear rate. As a result, the aforementioned proportionality is again observed.

Both studies in chapter 2 and 3 are closely related to a development of more general constitutive relation between deformation, concentration and stress, which can be extended to spatially inhomogeneous flow situation. The results of this thesis suggest detailed expression of mass and momentum transport coefficients in terms of microstructure of particulate suspension under various concentration and deformation rate.

Though both studies do not take account of the multi-body hydrodynamic interaction between particles in order to simplify the complicated non-uniform flow, fortunately, the modeling predictions show very acceptable match with the experimental result or the particle simulation. Such accordance might be valid until the hydrodynamic interaction is not crucial, for example, in case the concentration is sufficiently low or high, or the inter-particle force is the dominant force exerted on the particle.

The exact effects of the hydrodynamic interactions, which may complement the accuracy of the predictions made by this thesis, can be done by more rigorous theoretical analysis or enhanced particle simulation methods including hydrodynamic momentum coupling between particle and surrounding solvent, for examples, multi-particle collision dynamics, lattice Boltzmann, or dissipative particle dynamics. In those

simulation with inclusion of hydrodynamic interaction, it would also be worthwhile to investigate not only the effect of hydrodynamic interaction between particles, but also the hydrodynamic effect of wall to the suspending particles, so that the stick–slip boundary condition at the walls may lead to huge velocity gradient, which means considerable contribution of the non–local effects.

On the other hand, still an unanswered question remains; The framework used in this thesis is only focused on particulate suspension dispersed in Newtonian medium. However, as mentioned in chapter 2, many complex flows, for example, shear banding instability, are results of not only viscous effect like severe shear thinning, but also coupling with elastic effect of macromolecules consisting the soft matter system. Although some traditional Maxwell type constitutive models contain non–local contribution or coupling with concentration/configuration of micro–structure, those models are limited in ad–hoc phenomenological level. Therefore, the next step toward more widely applicable model should incorporate the viscoelastic behaviors of suspensions. In this case, the simple modeling, as treated in chapter 3, may not valid due to the complicity and non–linearity, but, some advanced particle simulation including viscoelastic effect may help in the future study.

References

- [1] J. K. G. Dhont, *An Introduction to Dynamics of Colloids*, edited by D. Mobius and R. Miller (Elsevier, Amsterdam, 1996)
- [2] R. G. Larson, *The Structure and Rheology of Complex Fluids* (Oxford University Press, New York, 1999)
- [3] W. B. Russel and W. R. Schowalter, *Colloidal Dispersions* (Cambridge University Press, Cambridge, 1989)
- [4] J. Mewis and N. J. Wagner, *Colloidal suspension rheology* (Cambridge University Press, Cambridge, 2011)
- [5] S. M. Fielding, *Soft Matter*, 3, 1262 (2007)
- [6] J. K. G. Dhont, *Phys. Rev. E*, 60,4534 (1999)
- [7] H. Jin, K. Kang, K. H. Ahn, W. J. Briels and J. K. G. Dhont, *J. Chem. Phys.*, 149, 014903 (2018)
- [8] A. Groisman, S.R. Quake, *Phys. Rev. Lett.* 92, 094501 (2004)
- [9] L.E. Rodd et al., *J. Non-Newtonian Fluid Mech.* 129,1 (2005)
- [10] C. E. Masselon, J.-P. Salmon, and A. Colin, *Phys. Rev. Lett.* 100, 038301 (2008)
- [11] H. Mohammadigoushki and S. J. Muller, *Soft Matter*, 12, 1051 (2016)
- [12] J. K. G. Dhont, Kyongok Kang, M.P. Lettinga and W. J. Briels, *Korea Aust. Rheol. J.*, 22, 291 (2010)
- [13] P. D. Olmsted, *Curr. Opin. Colloid Interface Sci.*, 4, 95 (1999)
- [14] J. Vermant, *Curr. Opin. Colloid Interface Sci.*, 6, 489 (2003)
- [15] M. E. Cates and S. M. Fielding, *Adv. Phys.*, 55, 799 (2006)
- [16] J. K. G. Dhont and W. J. Briels, *Rheol. Acta*, 47, 257 (2008)

- [17] K. Kang, M. P. Lettinga, Z. Dogic and J. K. G. Dhont, *Phys. Rev. E*, 74, 026307 (2006)
- [18] M. A. Fardin, T. J. Ober, C. Gay, G. Gregoire, G. H. McKinley and S. Lerouge, *Eur. Phys. J. E*, 96, 4404 (2011)
- [19] M. A. Fardin, B. Lasne, O. Cardoso, G. Gregoire, M. Argentina, J. P. Decruppe and S. Lerouge, *Phys. Rev. Lett.*, 103, 028302 (2009)
- [20] M. A. Fardin, D. Lopez, J. Croso, G. Gregoire, O. Cardoso, G. H. Mckinley and S. Lerouge, *Phys. Rev. Lett.*, 104, 178303 (2010)
- [21] P. Nozieres and D. Quemada, *Europhys. Lett.*, 2, 129. (1986)
- [22] V. Schmitt, C. M. Marques and F. Lequeux, *Phys. Rev. E*, 52, 4009 (1995)
- [23] R. Besseling, L. Isa, P. Ballesta, G. Petekidis, M. E. Cates and W. C. K. Poon, *Phys. Rev. Lett.*, 105, 268301 (2010)
- [24] J. F. Morris and F. Boulay, *J. Rheol.*, 43, 1213 (1999)
- [25] Y. Yurkovetsky and J. F. Morris, *J. Rheol.*, 52, 141 (2008)
- [26] A. Deboeuf, G. Gauthier, J. Martin, Y. Yurkovetsky and J. F. Morris, *Phys. Rev. Lett.*, 102, 108301 (2009)
- [27] D. R. Foss and J. F. Brady, *J. Rheol.*, 44, 629 (2000)
- [28] P. R. Nott and J. F. Brady, *J. Fluid Mech.*, 275, 157 (1994)
- [29] B. Garcia-Rojas, F. Bautista, J. E. Puig and O. Manero, *Phys. Rev. E*, 80, 036313 (2009)
- [30] D. Leighton and A. Acrivos, *J. Fluid Mech.*, 181, 415 (1987)
- [31] A. Acrivos, G. K. Batchelor, E. J. Hinch, D. L. Koch and R. Mauri, *J. Fluid Mech.*, 240, 651 (1992)
- [32] D. Wogerere, J. F. Morris and E. R. Weeks, *J. Fluid Mech.*, 581, 437 (2007)
- [33] D. A. McQuarrie, *Statistical Mechanics* (Harper & Row Publishers, 1973)

- [34] C. G. de Kruif, E. M. F. van Iersel, A. Vrij and W. B. Russel, *J. Chem. Phys.*, 83, 4717 (1985)
- [35] G. N. Choi and I. M. Krieger, *J. Colloid Interface Sci.*, 113, 101 (1986)
- [36] D. R. Foss and J. F. Brady, *J. Fluid Mech.*, 407, 167. (2000)
- [37] Z. Cheng, J. Zhu, P. M. Chaikin, S.-E. Phan and W. B. Russel, 65, 041405 (2002)
- [38] A. J. Banchio, J. Bergenholtz and G. Nagele, *Phys. Rev. Lett.*, 82, 1792 (1999)
- [39] I. M. Krieger, *J. Colloid Interface Sci.*, 3, 111 (1972)
- [40] J. C. van der Werff and C. G. de Kruif, *J. Rheol.*, 33, 421. (1989)
- [41] E. J. Saltzman and K. S. Schweizer, *J. Chem. Phys.*, 119, 1197 (2003)
- [42] J. Goyon, A. Colin, G. Ovarlez, A. Ajdari and L. Bocquet, *Nature*, 454, 84 (2008)
- [43] K. N. Pham, G. Petekidis, D. Vlassopoulos, S. U. Egelhaaf, W. C. K. Poon and P. N. Pusey, *J. Rheol.*, 52, 649 (2008)
- [44] N. F. Carnahan and K. E. Starling, *J. Chem. Phys.*, 51, 635 (1969)
- [45] M. D. Rintoul and S. Torquato, *J. Chem. Phys.*, 105, 9258 (1996)
- [46] J. W. Cahn and J. E. Hilliard, *J. Chem. Phys.*, 28, 258 (1958)
- [47] J. W. Cahn and J. E. Hilliard, *J. Chem. Phys.*, 31, 688 (1959)
- [48] P. Moin, *Fundamentals of Engineering Numerical Analysis* (Cambridge University Press, New York, 2nd edn, 2010)
- [49] P. D. Olmsted and C.-Y. D. Lu, *Phys. Rev. E*, 56, 55 (1997)
- [50] P. D. Olmsted and C.-Y. D. Lu, *Phys. Rev. E*, 60, 4397 (1999)
- [51] H. Jin, K. Kang, K. H. Ahn and J. K. G. Dhont, *Soft Matter* 10, 9470 (2014).

- [52] G. Zhu, H. Rezvantalab, E. Hajizadeh, X. Wang, and R. G. Larson, *J. Rheol.* 60, 327 (2016)
- [53] A. W. El-Kareh and L. G. Leal, *J. NonNewtonian Fluid Mech.* 33, 257 (1989)
- [54] A. V. Bhave, R. C. Armstrong, and R. A. Brown, *J. Chem. Phys.* 95, 2988 (1991)
- [55] X.-F. Yuan, *Europhys. Lett.* 46, 542 (1999)
- [56] C.-Y. D. Lu, P. D. Olmsted, and R. C. Ball, *Phys. Rev. Lett.* 84, 642 (2000)
- [57] O. Radulescu, P. D. Olmsted, J. P. Decruppe, S. Lerouge, J.-F. Berret, and G. Porte, *Europhys. Lett.* 62, 230 (2003)
- [58] S. M. Fielding, *Phys. Rev. Lett.* 95, 134501 (2005)
- [59] S. M. Fielding, *Phys. Rev. E* 76, 016311 (2007)
- [60] P. D. Olmsted and C.-Y. D. Lu, *Faraday Discuss.* 112, 183 (1999)
- [61] J. K. G. Dhont and W. J. Briels, *J. Chem. Phys.* 117, 3992 (2002)
- [62] G. K. Batchelor, *J. Fluid Mech.* 41, 545 (1970)
- [63] G. K. Batchelor, *J. Fluid Mech.* 83, 97 (1977)
- [64] A. van den Noort and W. J. Briels, *Macromol. Theory Simul.* 16, 742 (2007)
- [65] A. van den Noort and W. J. Briels, *J. Non-Newtonian Fluid Mech.* 152, 148 (2008)
- [66] J. Sprakel, J. T. Padding, and W. J. Briels, *Europhys. Lett.* 93, 58003 (2011)
- [67] M. Schindler, *Chem. Phys.* 375, 327 (2010)
- [68] P. J. Carreau, *Trans. Soc. Rheol.* 16, 99 (1972)
- [69] B. J. Alder and T. E. Wainwright, *Phys. Rev. A* 1, 18 (1970)

국문 초록

불균일한 유동장은 다양한 복잡 전달 현상에 영향을 미친다. 불균일 유동은 입자계 현탁액을 이용한 여러 산업 공정 유동이나 미세관 유동 등 중요한 유동 상황들에서 필연적으로 나타나기 때문에 불균일 유동장 하에서 나타나는 전달 현상들을 이해하는 것은 중요하다고 할 수 있다. 그러나, 불균일 유동장 하에서 현탁액의 거동에 대한 연구는 아직 많이 이루어지지 못하였는데, 이는 불균일한 유동, 농도장에 대한 실험적 분석이 제한적이기 때문이다.

본 학위 논문에서는 불균일한 유동장 하에서 입자계 현탁액에 나타나는 물질 및 운동량 전달을 이론적 모델링 및 전산 모사 방법론을 사용하여 탐구하였다. 먼저, colloidal glass 시스템에서 나타나 shear rate gradient concentration coupling instability에 대해 다루었다. 이 유동 불안정 현상은 불균일한 유동장에 의해 유발된 입자의 물질 전달이 유체의 점도와 응력 균형에 영향을 주고 이로 인해 왜곡된 유동장이 다시 물질전달을 일으키는 증폭 상호작용에 의해 일어난다. 본문에서는 이 물질 전달이 일어나는 원인을 미시적 수준에서 규명하였다. 이 과정에서 입자의 물질전달 계수에 대한 표현식을 입자계의 미시 구조 인자에 대하여 나타내었다. 이어서, Brownian dynamics simulation을 이용해 여러 유동조건 하에서 입자계의 미시 구조를 계산하였고 이를 이용해 물질전달 계수들을 유동 조건인 변형률과 농도에 대한 함수로 얻어낼 수 있었다. 또한, 이렇게 유도된 물질전달 계수를 활용하여 유동 해석 시뮬레이션을 수행하여 본 유동 불안정 현상의 거동을 관찰하였다. 이때, 후술할 non-local stress가 중요한 역할을 하였다.

두 번째로, 입자계 현탁액에서 불균일한 유동장이 유발하는 추가적인 응력인 non-local stress에 대해 다루었다. Non-local stress는 유동 불안정 현상을 설명하거나 복잡 유체의 미세관 유동을 다룰 때 중요하게 작용하는 응

력이지만 입자계에서는 다루어진 바 없었다. 본 연구에서는 입자계 현탁액의 non-local stress를 유도하기 위해 우선 입자간 상호작용을 무시할 수 있는 묽은 현탁액에서 불균일 유동장에 수력학 모델링을 적용하여 non-local stress를 계산하였다. 그 결과, 묽은 용액에서의 점도식으로 잘 알려진 Einstein viscosity와 대응되는 non-local stress 항이 도출되는 것을 확인하였다. 이 결과를 더 복잡한 현탁액으로 확장하기 위해 effective medium 가정을 도입하였다. 이 가정은 복잡한 현탁액의 non-local stress가 묽은 현탁액에서와 마찬가지로 현탁액의 점도와 비례 관계를 가질 것이라는 가정이다. 이 가정의 타당성을 검증하기 위하여 Brownian dynamics simulation을 이용하여, shear thinning 거동을 보이는 현탁액에 불균일한 유동장을 가하였다. 불균일한 유동장 하에서 현탁액 내부의 local stress의 분포를 측정하여 non-local stress를 포함하는 구성방정식과 최소 자승(least squares regression) 회귀분석을 통해 현탁액의 non-local stress를 측정하였다. 그 결과, shear rate의 증가에 따른 shear thinning과 함께, non-local stress 계수의 감소가 정비례하게 나타났고, 이를 통해 앞서 도출한 Einstein analogy를 다시 한 번 확인할 수 있었다.

본 연구를 통하여 입자계 현탁액의 불균일한 유동장 하에서의 복잡 전달 현상에 대한 기초적인 이해를 돕고, 더 나아가 실제 복잡 유체의 공정의 개선에 도움을 줄 수 있을 것으로 기대된다.

주요어 : shear banding instability, 불균일 유동장, 입자계 현탁액, 물질 및 운동량 전달, 구성방정식, Brownian dynamics 시뮬레이션, 미세 구조

학번 : 2012-20980

Curriculum Vitae

Name: Howon Jin

Date of Birth: Sep. 27, 1990

Present Address: Bldg.311 #412, School of Chemical and Biological Engineering,
Seoul National University,
1 Gwanak-ro, Gwanak-gu, Seoul 08826, Korea
Email: jinjin927@snu.ac.kr
Tel: 82-2-880-1580

Education

- **Master and Ph.D. course**, Seoul National University, Korea
(03. 2012~02.2019)
Advisor: Prof. Kyung Hyun Ahn
- **Visiting research student:** Institute of Complex systems (ICS-3), Forschungszentrum
Jülich, Germany (02.2013~02.2014, 07.2015~08.2015, 06.2016~08.2016)
- **BS in Chemical and Biological Engineering**, Seoul National University, Korea
(02.2012)

Publication

- A. Lee, H. Jin, H. W. Dang, K. H. Choi and K. H. Ahn, "Optimization of experimental parameters to determine the jetting regimes in electrohydrodynamic printing", *Langmuir*, 2013
- H. Jin, K. Kang, K. H. Ahn and J. K. G. Dhont, "Flow instability due to coupling of shear-gradients with concentration: non-uniform flow of (hard-sphere) glasses", *Soft Matter*, 2014
- H. Jin, K. Kang, K. H. Ahn, W. J. Briels and J. K. G. Dhont, "Non-local stresses in highly non-uniformly flowing suspensions: The shear-curvature viscosity", *The Journal of Chemical Physics*, 2018

Research experience

- **Simulation on suspension rheology (local/bulk stress, structure analysis)**
Brownian dynamics simulation
Self-Consistent particle simulation method (Myung et. al., JNNFM, 2011)
Smoothed particle hydrodynamics simulation
Hydrodynamically coupled Brownian dynamics simulation
- **Finite element method simulation:**
Study on FEM codes for stokes flow, heat equation and mass transfer
- **Computational language:**
FORTRAN, C (some), MATLAB (image processing)

Award

- KChO(Korea Chemistry Olympiad), Grand prize (2006)
- Campus Patent Strategy Universiade, participation prize (2010)
- 23rd Korea Chemical Engineering Universiade (transport phenomena), bronze prize (2011)
- Spring meeting of The Korean Society of Rheology, Excellent paper award – oral presentation (2014)
- Dongjin Excellent paper award (2018, by Dongjin Semichem Co., Ltd.)

Other experience

- **Scholarship**
Presidential science scholarship (2008.03 – 2012.02)
- **Teaching Assistant:**
Process fluid mechanics (2012.03 - 2012.06)
Heat and mass Transfer (2012.09 - 2012.12)
Transport phenomena (2014.03 - 2014.06)

International conferences

1. (Poster presentation) Howon Jin and Kyung Hyun Ahn, Evolution of particle distribution profile in the pressure driven microchannel flow of particulate suspensions, The 16th International Congress on Rheology(ICR), Lisbon, Portugal (5-10. Aug. 2012)
2. (Participation only) The Annual European Rheology Conference (AERC), Leuven, Belgium (2-5. Apr. 2013)
3. (Poster presentation) Howon Jin, Kyong-ok Kang, Kyung Hyun Ahn and Jan K. G. Dhont, Numerical simulation on SCC (shear-rate gradient concentration coupling) instability of colloidal spheres, International Soft Matter Conference(ISMC), Rome, Italy (15-19. Sep. 2013)
4. (Poster presentation) Howon Jin, Kyongok Kang, Kyung Hyun Ahn, and J.K.G. Dhont, Shear-rate gradient concentration coupling instability of hard sphere glasses: Modeling and simulation, Juelich Soft Matter Days 2014, Bad Honnef, Germany (11-14. Nov. 2014)
5. (Oral presentation) Howon Jin, Kyong-ok Kang, Kyung Hyun Ahn and Jan K. G. Dhont , Concentration coupled flow instability of hard sphere glasses : modeling and simulation, The Society of Rheology 87th Annual Meeting(SoR), Baltimore, U.S.A.(11-15. Oct. 2015)
6. (Oral presentation) Howon Jin, Kyong-Ok Kang, Kyung Hyun Ahn, Wim J. Briels, Jan K. G. Dhont, Non-local stresses in colloidal suspensions: modeling and simulation, The Annual European Rheology Conference (AERC), Copenhagen, Denmark, (3-6, Apr. 2017)
7. (Oral presentation) Howon Jin, Kyung Hyun Ahn, Effect of non-local stress on shear banding flow in confined geometry: Numerical simulation and rheological measurement, The Annual European Rheology Conference (AERC), Sorrento, Italy, (17-20, Apr. 2018)
8. (Oral presentation) Howon Jin, Kyung Hyun Ahn, Numerical study on shear banding flow in confined geometry: Effect of non-local stress and confinement, The 7th Pacific Rim Conference on Rheology, Jeju, Korea, (10- 15. June 2018)

Reference

1. Prof. Kyung Hyun Ahn (Ph.D. Advisor)
School of Chemical and Biological Engineering, Seoul National University,
Gwanak-ro, Gwanak-gu, Seoul 08826, Korea
Tel: +82-2-880-1897
Email: ahnnet@snu.ac.kr
2. Prof. Jan K. G. Dhont
Institute of Complex Systems, Forschungszentrum Juelich,
52425 Juelich, Germany
Email: j.k.g.dhont@fz-juelich.de